JfM PAPERS

On the rheology and magnetization of dilute magnetic emulsions under small amplitude oscillatory shear

Rodrigo F. Abdo[1,2,†], **Victor G. Abicalil**[1,†], **Lucas H.P. Cunha**[3,4,†] and **Taygoara F. Oliveira**[1,†]

[1]Laboratory of Energy and Environment, Department of Mechanical Engineering, University of Brasília, Brasília, DF 70910-900, Brazil

[2]Federal Institute of Brasília - Estrutural Campus, Brasília, DF 71250-000, Brazil

[3]Department of Chemical and Biomolecular Engineering, Rice University, Houston, TX 77005, USA

[4]Center for Theoretical Biological Physics, Rice University, Houston, TX 77005, USA

A dilute magnetic emulsion under the combined action of a uniform external magnetic field and a small amplitude oscillatory shear is studied using numerical simulations. We consider a three-dimensional domain with a single ferrofluid droplet suspended in a non-magnetizable Newtonian fluid. We present results of droplet shape and orientation, viscoelastic functions and bulk emulsion magnetization as functions of the shear oscillation frequency, magnetic field intensity and orientation. We also investigate how the magnetic field induces mechanical anisotropy by producing internal torques in oscillatory conditions. We found that, when the magnetic field is parallel to the shear plane, the droplet shape is mostly independent of the shear oscillation frequency. Regarding the viscometric functions, we show how the external magnetic field modifies the storage and loss moduli, especially for a field aligned to the main velocity gradient. The bulk emulsion magnetization is studied in the same fashion as the viscoelastic functions of the oscillatory shear. We show that the in-phase component of the magnetization with respect to the shear rate reaches a saturation magnetization, at the high frequencies limit, dependent on the magnetic field intensity and orientation. On the other hand, we found a non-zero out-of-phase response, which indicates a finite emulsion magnetization relaxation time. Our results indicate that the magnetization relaxation is closely related to the mechanical relaxation for dilute magnetic emulsions under oscillatory shear.

Key words: drops, rheology, emulsions

† Email addresses for correspondence: rodrigo.abdo@ifb.edu.br, victorabicalil@gmail.com, lh36@rice.edu, taygoara@unb.br

1. Introduction

Knowledge of emulsion rheology is critical for many purposes, such as improving the delivery of active pharmaceutical ingredients (Jaiswal, Dudhe & Sharma 2015), milk homogenization (Bai *et al.* 2021) or improving the quality of cosmetic products (Kim, Oh & Lee 2020). Despite emulsions usually being composed of Newtonian fluids, the bulk material behaves as a single non-Newtonian fluid due to the droplets dynamics in the microstructure, revealing a broad spectrum of behaviours, ranging from elastic to plastic.

Unlike some authors, who described the droplet dynamics in simple shear flows (Taylor 1932; Kennedy, Pozrikidis & Skalak 1994; Maffettone & Minale 1998; Vananroye, Van Puyvelde & Moldenaers 2006; Ioannou, Liu & Zhang 2016), Palierne (1990) studied the linear viscoelastic behaviour of dilute and non-dilute emulsions by using small amplitude oscillatory shear flows. This model is recognized to accurately describe molten polymer blends at high and low frequencies (Bousmina 1999). His theory also generalizes the previous approaches of Fröhlich & Sack (1946), Oldroyd & Wilson (1950, 1953), Oldroyd & Taylor (1955) and Kerner (1956).

Cavallo, Guido & Simeone (2003) and Wannaborworn, Mackley & Renardy (2002) investigated the dynamics of single droplets in small amplitude oscillatory shear flows. They reported that the droplet deforms following an ellipsoidal shape. Once the flow is reversed, the droplet is compressed in the major axis and extended in the minor axis, approaching a spherical shape between the shear cycles. In contrast to the large amplitude oscillatory shear cases, the nature of droplet oscillation angle does not change as the frequency increases (Guido, Grosso & Maffettone 2004).

Oliveira & Cunha (2015), using the boundary integral method (Siqueira *et al.* 2017; Cunha *et al.* 2018*a*; De Siqueira *et al.* 2018) and an asymptotic solution based on the small deformation theory (Vlahovska, Błazwdziewicz & Loewenberg 2009), reported a rheological study on droplets of moderate to high viscosity ratios subjected to oscillatory shear flows, showing that the system dynamics depends on the shear rate, oscillation frequency and droplet relaxation time. They observed that, for a dilute emulsion, large oscillation amplitudes might lead to non-harmonic responses of the shear stresses and nonlinear behaviours.

Emulsions can be manipulated in many ways, but due to the high surface energy of the interface, they are thermodynamically unstable (Maphosa 2018). One alternative to make these structures stable is to use surfactants in an attempt to reduce the interfacial tension. In turn, the transport of surfactants over the droplet surface leads to complex rheological responses of the droplet (Pimenta & Oliveira 2021). Another technology that has gained attention is known as Pickering emulsions, in which solid particles are used to stabilize and tune the surface properties (Jiang, Sheng & Ngai 2020). In both cases, it is necessary to introduce an additional substance into the system. Another different way to actively control an emulsion arises for a ferrofluid as a disperse phase (Cunha *et al.* 2018*b*, 2020*b*; Ishida & Matsunaga 2020; Abicalil *et al.* 2021).

The manipulation of emulsions in which the dispersed phase is composed of ferrofluid droplets by the application of external magnetic fields has been extensively studied in the past years due to the promising applications in medical treatments (Voltairas, Fotiadis & Massalas 2001; Mefford *et al.* 2007; Liu, Li & Lam 2018), development of externally controlled materials (Dierking *et al.* 2020; Spatafora-Salazar *et al.* 2021; Ishida *et al.* 2022) and applications in Lab-on-a-chip devices (Varma *et al.* 2016; Ray *et al.* 2017; Sen *et al.* 2017; Zhang *et al.* 2019). The interaction with external magnetic fields permits an active control of the material's rheology (Abicalil *et al.* 2021; Cunha *et al.* 2018*b*, 2020*b*; Ishida & Matsunaga 2020), its manipulation in confined systems

(Bijarchi *et al.* 2020, 2021; Roodan *et al.* 2020) and might be used for the design of actively controlled heat transfer devices (Cunha *et al.* 2020*a*). Furthermore, recent studies have proposed the use of ferrofluid droplets as liquid microrobots for targeted cargo delivery in microsystems (Fan *et al.* 2020*a*,*b*; Chen *et al.* 2021; Ji *et al.* 2021).

Recently, Abicalil *et al.* (2021) expanded the works of Cunha *et al.* (2018*b*, 2020*b*) and Ishida & Matsunaga (2020), and investigated magnetic emulsions in simple shear flows. The authors analysed the droplet geometry, rheology, bulk magnetization and magnetic torque for external magnetic fields applied in different directions. According to such works, depending on the field orientation with respect to the flow, the effective viscosity of the system can be either increased or decreased, as well as the first and second normal stress differences. Moreover, although the ferrofluid droplet is assumed to be superparamagnetic, the coupled shear and magnetic effects induce a misalignment between the droplet magnetization and the applied magnetic field. As a consequence, the system experiences an induced magnetic torque which leads to asymmetries in the bulk stress tensor.

Several recent studies have addressed the issue of the droplet dynamics under a uniform external magnetic field (Hassan, Zhang & Wang 2018; Jesus, Roma & Ceniceros 2018; Hassan & Wang 2019), and others on the rheology and magnetization of ferrofluid emulsions under simple shear (Cunha *et al.* 2018*b*, 2020*b*; Ishida & Matsunaga 2020; Abicalil *et al.* 2021; Capobianchi *et al.* 2021). Additionally, considerable research attention has been directed towards complex structures formed by magnetizable suspended particles under simple shear or oscillatory shear (Rosa & Cunha 2019, 2020; Cunha & Rosa 2021). To the best of the authors' knowledge, no such studies have explored the role of the external magnetic field in the rheology and magnetization of dilute emulsions subjected to a small amplitude oscillatory shear (SAOS).

In this work, we present a numerical analysis of the rheology and magnetization of a ferrofluid droplet under the combined action of a magnetic field and a SAOS. We consider a three-dimensional domain with a single ferrofluid droplet suspended in a non-magnetizable Newtonian matrix fluid, compatible with the dilute regime. The presented numerical approach uses the projection method to solve the Navier–Stokes equations with body force terms to account for interfacial and magnetic forces, the magnetostatic Maxwell equations to solve the magnetic field throughout the domain and the level set method for interface capturing. Although it is well known that droplet interactions are an essential part of the study of concentrated emulsions, the study of dilute emulsions reveals fundamental mechanisms of the nature of these materials. Thus, several authors (Raja, Subramanian & Koch 2010; Ghigliotti, Biben & Misbah 2010; Vlahovska 2011; Mandal *et al.* 2018; Poddar *et al.* 2019; Guido & Shaqfeh 2019) have studied the rheology of dilute emulsions, mainly considering a single droplet dispersed in volumetric fractions of up to 5 % (Guido & Shaqfeh 2019).

We studied the effects of a uniform external magnetic field on the behaviour of a dilute emulsion of ferrofluid droplets, under oscillatory shear flows. We explored the morphological characteristics of the droplet between the limits of low and high oscillation frequencies in order to describe the viscoelastic properties and the ability of the magnetic field to produce anisotropy. Furthermore, we studied the oscillatory magnetic torque produced by the misalignment angle between the emulsion's bulk magnetization and the external magnetic field. We found that the magnetic field can considerably modify the behaviour of the storage and loss moduli as functions of the oscillation frequency, even changing the flow dynamics when the external field is oriented perpendicular to the shear plane. Finally, we show how the complex interactions between surface tension, shear stress

and magnetic field produce a finite magnetic relaxation time, even though the ferrofluid inside the droplets is superparamagnetic.

The remainder of this work is organized as follows: in § 2, we present the problem statement, including the governing equations and the non-dimensional parameters that govern the model problem. Section 3 presents the numerical methodology used to solve the governing equations. Results and discussions are presented in § 4, with concluding remarks presented in § 5.

2. Problem statement

The problem under consideration consists of a ferrofluid droplet suspended in a non-magnetizable viscous fluid. The system is confined in a channel between two parallel plates. The upper and lower plates oscillate in opposite directions with angular velocity ω, creating an oscillatory shear flow in the system with shear-rate amplitude $\dot{\gamma}_0$. Moreover, the ferrofluid droplet interacts with an external uniform magnetic field H_0, which can be parallel to either the main flow direction (x), the main velocity gradient direction (y) or the main vorticity direction (z). The continuous phase has magnetic permeability μ_0, assumed to be equal to that of free space, while the dispersed phase has magnetic permeability $\zeta \mu_0$, where $\zeta = \mu_d/\mu_0$ is the magnetic permeability ratio. Both phases have the same viscosity η and density ρ. The droplet's surface is assumed to be free of tensioactive substances, such that it has a constant surface tension coefficient σ.

The computational model consists of a rectangular domain of dimensions L_x, L_y and L_z, in which the droplet is initially spherical with radius a and placed at the centre. The boundaries normal to the y-direction represent parallel plates oscillating in opposite directions with angular velocity ω, such that the upper wall has a velocity $u = \dot{\gamma}_0 \cos{(\omega t)} L_y/2$, while all other boundaries are assumed to be periodic. A schematic illustration of the problem is presented in figure 1 for the external magnetic field in the main velocity gradient direction.

The magnetic problem is assumed to be quasi-stationary, such that no electric currents are induced. Therefore, in the absence of electric fields, Maxwell's equations reduce to $\nabla \cdot B = 0$ and $\nabla \times H = 0$, where B is the induction field and H is the magnetic field. Here, we assume the ferrofluid as superparamagnetic (Rosensweig 2013), such that magnetization is given by $M = \chi H$, with a constant magnetic susceptibility χ. In this way, the magnetic induction can be written as $B = \mu_0(H + M)$. Defining the permeability function $\zeta_\phi(x)$ such that $\zeta_\phi(x) = 1$ in the continuous phase and $\zeta_\phi(x) = 1 + \chi$ inside the droplet, we may extend the relation $B = \mu_0 \zeta_\phi H$ to the entire domain. Since the magnetic field is irrotational, it can be written as the gradient of the magnetic potential field ψ, such that $H = -\nabla \psi$. As B is solenoidal, the magnetic potential field is given by

$$\nabla \cdot (\zeta(x)\nabla \psi) = 0. \tag{2.1}$$

In a continuous perspective, the hydrodynamic problem for the immiscible two-fluid system is governed by the incompressible Navier–Stokes equations, accounting for the magnetic and capillary forces as body forces per unit of volume, represented as F_m and F_i, respectively. Thus,

$$\rho \left(\frac{\partial u}{\partial t} + u \cdot \nabla u \right) = -\nabla P + \nabla \cdot (2\eta D) + F_i + F_m, \tag{2.2}$$

$$\nabla \cdot u = 0, \tag{2.3}$$

where u is the velocity field, t is time, P is the pressure and $D = (\nabla u + \nabla u^{\mathrm{T}})/2$ is the strain-rate tensor. The introduction of the level set function $\phi(x)$, which is a signed distance
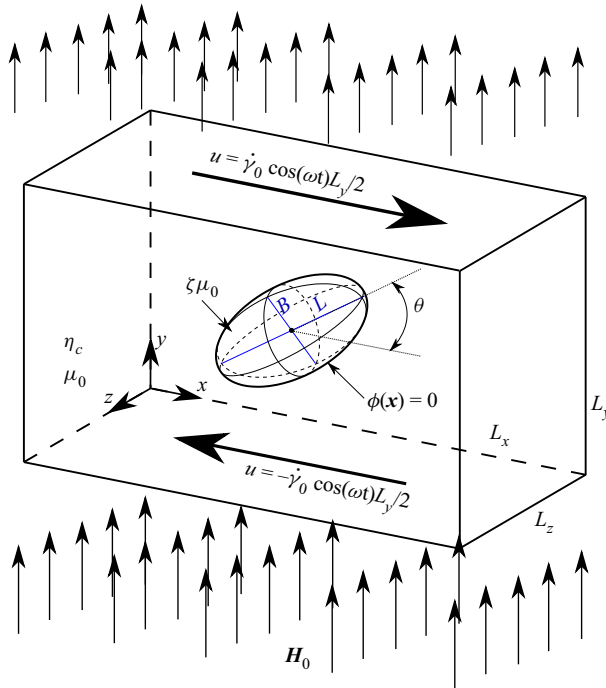
Figure 1. Schematic illustration of the problem for the external magnetic field, $\boldsymbol{H}_0$, parallel to the main velocity gradient direction (y). The domain is of finite size $L_x \times L_y \times L_z$. The magnetic permeabilities of the continuous and the ferrofluid phases are, respectively, μ_0 and $\zeta\mu_0$. A shear flow is imposed on the system by the top and bottom walls moving in opposite directions with velocity $u = \dot{\gamma}_0 \cos(\omega t)L_y/2$. The droplet surface is determined by the level-set function $\phi(\boldsymbol{x}) = 0$. The droplet is shown in a deformed state with major and minor axis lengths L and B, respectively. The droplet's inclination angle is θ.

function to the fluids' interface (as further discussed in § 3.1), allows the magnetic and capillary forces to be described as (Sussman *et al.* 1998; Cunha *et al.* 2018*b*)

$$\boldsymbol{F}_i = -\sigma\kappa(\phi)\delta(\phi)|\nabla\phi|\hat{\boldsymbol{n}}, \tag{2.4}$$

and

$$\boldsymbol{F}_m = \mu_0(\zeta_\phi(\phi) - 1)\boldsymbol{H} \cdot \nabla\boldsymbol{H}, \tag{2.5}$$

where κ is the local mean curvature, δ is the Dirac delta function and $\hat{\boldsymbol{n}}$ is the unit normal vector, pointing outwards of the droplet surface.

We normalize the formulation using a for length, $\eta a/\sigma$ for time (droplet relaxation time), σ/η for velocity, σ/a for pressure and tension and $|\boldsymbol{H}_0|$ for magnetic field and magnetization. The tilde notation is used to represent non-dimensional variables. While (2.3) remains the same in non-dimensional form, (2.2) is rewritten as

$$\begin{aligned}
\frac{\partial\tilde{\boldsymbol{u}}}{\partial\tilde{t}} + \tilde{\boldsymbol{u}} \cdot \tilde{\nabla}\tilde{\boldsymbol{u}} = &-\frac{Ca}{Re}\tilde{\nabla}\tilde{P} + \frac{Ca}{Re}\tilde{\nabla} \cdot (2\tilde{\boldsymbol{D}}) \\
&- \frac{Ca}{Re}\tilde{\kappa}(\phi)\tilde{\delta}(\phi)|\tilde{\nabla}\phi|\hat{\boldsymbol{n}} \\
&+ \frac{Ca\,Ca_{mag}}{Re}(\tilde{\zeta}_\phi(\phi) - 1)\tilde{\boldsymbol{H}} \cdot \tilde{\nabla}\tilde{\boldsymbol{H}}.
\end{aligned} \tag{2.6}$$

As the characteristic dimensionless groups governing the problem, we have: the Reynolds number, $Re = \rho\dot{\gamma}_0 a^2/\eta$, which measures the ratio between inertial and viscous effects; the capillary number, $Ca = \dot{\gamma}_0 a\eta/\sigma$, corresponding to the ratio between viscous and capillary forces; and the magnetic capillary number, $Ca_{mag} = \mu_0 H_0^2 a/\sigma$, as the ratio between magnetic and capillary forces.

The oscillatory motion, as illustrated in figure 1, is applied to both plates normal to the *y*-direction, in opposite directions, according to the non-dimensional equation $\tilde{U} = \pm Ca\cos(\tilde{\omega}\tilde{t})\tilde{L}_y/2$. The shear strain produced in the system by the plate displacement is $\tilde{\gamma} = \tilde{\gamma}_0\sin(\tilde{\omega}\tilde{t})$, where $\tilde{\gamma}_0 = Ca/\tilde{\omega}$ is the strain amplitude. Both pressure and velocity fields are taken as periodic at the boundaries normal to the *x* and *z*-directions. The uniform external magnetic field is applied according to the chosen direction (*x*, *y* or *z*) by imposing Neumann boundary conditions to the magnetic potential on all domain boundaries, such that $\tilde{\nabla}\psi = -\tilde{H}_0$.

For the remainder of this text, all presented variables are non-dimensional and the tilde symbol is suppressed to alleviate the notation.

3. Methodology

Following the Helmholtz–Hodge decomposition (Bhatia *et al.* 2013) and the original projection method developed by Chorin (1968) and Témam (1969*a*,*b*), we use a second-order semi-backward difference formula as described by Badalassi, Ceniceros & Banerjee (2003). This semi-implicit method works quite well for diffusion-dominated equations. It consists of adding and subtracting the diffusive term in the current time, treating one term implicitly and the other explicitly. The first step consists of solving the following equation for $\boldsymbol{u}^*$, ignoring the pressure field:

$$\left.\begin{aligned} \frac{1}{2\Delta t}\left(3\boldsymbol{u}^* - 4\boldsymbol{u}^n + \boldsymbol{u}^{n-1}\right) - \frac{Ca}{Re}\nabla^2\boldsymbol{u}^* = -\frac{Ca}{Re}\nabla^2\hat{\boldsymbol{u}} \\ -\hat{\boldsymbol{u}}\cdot\nabla\hat{\boldsymbol{u}} + \frac{Ca}{Re}\nabla\cdot(2\hat{\boldsymbol{D}}) + \boldsymbol{F}_i(\hat{\phi}) + \boldsymbol{F}_m(\hat{\phi},\hat{H}), \end{aligned}\right\} \quad (3.1)$$

where the hat symbol (ˆ) corresponds to an approximation of $\boldsymbol{u}^{n+1}$ using the second-order formula $\hat{\boldsymbol{u}} = 2\boldsymbol{u} - \boldsymbol{u}^{n-1}$. The second step projects $\boldsymbol{u}^*$ onto the space of divergence-free velocities according to

$$\boldsymbol{u}^{n+1} = \boldsymbol{u}^* - \frac{2Ca\Delta t}{3Re}\nabla\left(p^{n+1}\right), \quad (3.2)$$

where the virtual pressure p^{n+1} is calculated taking the divergence of (3.2), leading to the Poisson equation

$$\nabla^2 p^{n+1} = \frac{3Re}{2Ca\Delta t}\nabla\cdot\boldsymbol{u}^*. \quad (3.3)$$

Combining (3.1), (3.2) and (3.3) we obtain an equation for the pressure in the form

$$P^{n+1} = p^{n+1} - \nabla\cdot\boldsymbol{u}^*. \quad (3.4)$$

All cases reported here were performed using a regular, staggered marker and cell (Harlow & Welch 1965) grid, with centred second-order finite differences for all terms in (2.1) and (3.1), except for the advective term, which uses a conservative upwind discretization, where the biased derivatives are calculated using a second-order essentially non-oscillatory scheme with upwinding (Osher & Sethian 1988). While (3.1) and (3.3)

are solved with a fast Poisson solver based on Fourier analysis and Gaussian elimination (Dodd & Ferrante 2014; Costa 2018), (2.1) is solved using a conjugate gradient algorithm with multigrid preconditioning (McAdams, Sifakis & Teran 2010).

3.1. *Level-set method*

Osher & Sethian (1988) proposed the level-set method based on the implicit description of surfaces so that the interface has a codimension one (Osher & Fedkiw 2003). The level-set function can be chosen to be any Lipschitz continuous function, although a signed distance function improves geometrical parameters and properties such as mass conservation (Gibou, Fedkiw & Osher 2018). In this way, the level-set function, $\phi(\mathbf{x})$, is defined as a signed distance function from the interface, taken as positive for points outside the droplet, and negative for points inside of it. In the level-set method, the distance function is assumed to be a material property, conserved by the fluid particles. In this sense, as in the continuum mechanics framework, the particles in the interface are always the same ones, and the droplet surface can be implicitly tracked by finding the Eulerian points where $\phi(\mathbf{x}) = 0$. Since ϕ is conserved by the material particles, the evolution of the interface is given by

$$\frac{\partial \phi}{\partial t} + \mathbf{u} \cdot \nabla \phi = 0. \tag{3.5}$$

Following this construction, the unit normal vector is calculated as $\hat{\mathbf{n}} = \nabla\phi/|\nabla\phi|$, and the local mean curvature as $\kappa = \nabla \cdot \hat{\mathbf{n}}$.

In the level-set method, a sharp interface is replaced by a smoothed one with a finite thickness of 2ε, where ε is defined according to the size of a grid cell ($\varepsilon = 1.5\Delta x$). In this way, the fluid properties can be determined according to a smoothed Heaviside function, such as the continuous magnetic permeability: $\zeta_\phi(\phi) = \zeta + (1 - \zeta)H_\varepsilon(\phi)$, where H_ε is given by

$$H_\varepsilon(\phi) = \begin{cases} 0, & \text{if } \phi < -\varepsilon, \\ \dfrac{1}{2}\left[1 + \dfrac{\phi}{\varepsilon} - \dfrac{1}{\pi}\sin(\pi\phi/\varepsilon)\right], & \text{if } |\phi| \leqslant \varepsilon, \\ 1, & \text{if } \phi > \varepsilon. \end{cases} \tag{3.6}$$

The smoothed Dirac delta function can then be defined as $\delta_\varepsilon(\phi) = \mathrm{d}H_\varepsilon(\phi)/\mathrm{d}\phi$.

As the interface moves according to (3.5), the level-set function does not retain its original properties and progressively deviates ϕ from the actual signed distance function. In this way, ϕ must be regularly recomputed (reinitialized) for all particles outside of the interface. We perform this reinitialization using the method of Peng *et al.* (1999) combined with the mass conservation correction algorithm developed by Sussman & Fatemi (1999). The reinitialization is performed at each time step by evolving the equation

$$\frac{\partial \phi}{\partial \tau} + s(\phi)(|\nabla\phi| - 1) - \lambda f(\phi) = 0, \tag{3.7}$$

in an artificial time, τ. The volume-preserving correction parameters, $\lambda f(\phi)$, and the signal function, $s(\phi)$, are defined, respectively, as

$$s(\phi) = \frac{\phi}{\sqrt{\phi^2 + |\nabla\phi|^2 \Delta x^2}}, \tag{3.8}$$

and

$$\lambda = \frac{\displaystyle\int_{\Omega} \delta(\phi)\,(s(\phi)(|\boldsymbol{\nabla}\phi| - 1))\,\mathrm{d}V}{\displaystyle\int_{\Omega} \delta(\phi)f(\phi)\,\mathrm{d}V}, \tag{3.9}$$

in which $f(\phi) = \delta(\phi)|\boldsymbol{\nabla}\phi|$ and Ω represents each individual grid cell, allowing the algorithm to locally correct variations in the droplet's volume. Furthermore, the steady solution of (3.7) assures that $|\boldsymbol{\nabla}\phi| = 1$, so ϕ recovers the actual signed distance function.

To solve (3.5) and (3.7), we use a fifth-order weighted essentially non-oscillatory scheme for spatial discretization (Jiang & Peng 2000), and a third-order strong stability-preserving Runge–Kutta scheme (Shu & Osher 1988; Gottlieb, Ketcheson & Shu 2011) for temporal evolution. Moreover, (3.5) uses an upwind scheme while (3.7) uses Godunov's method for spatial discretization (Gibou *et al.* 2018).

Note that, in the level-set framework, a surface integral over the interface Γ where $\phi = 0$ can be evaluated as a volume integral over the entire domain V, with the aid of the Dirac delta function, according to (Osher & Fedkiw 2003)

$$\int_{\Gamma} \mathfrak{F}(\boldsymbol{x})\,\mathrm{d}\Gamma = \int_{V} \mathfrak{F}(\boldsymbol{x})\delta_{\epsilon}(\phi)|\boldsymbol{\nabla}\phi|\,\mathrm{d}V, \tag{3.10}$$

where $\mathfrak{F}$ is an arbitrary function.

In this work, this volume integral is approximated with a second-order quadrature, using a 27-point stencil.

4. Results and discussions

In this section, we study the behaviour of a single ferrofluid droplet subjected to a SAOS, under the action of a uniform external magnetic field. First, we analyse the impact of the external magnetic field on both the droplet's deformation and inclination. The droplet's deformation is measured following Taylor's deformation parameter defined as $D = (L - B)/(L + B)$, where L and B are, the major and minor axes of the deformed droplet, respectively, as shown in figure 1. The inclination angle, θ, is defined as the angle between the major deformation direction and the x-axis. All geometrical measurements taken throughout this work are related to the droplet shape projected in the shear plane, i.e. the xy plane crossing the droplet's centre. Then, we focus on the effects of the external magnetic field on the storage and loss moduli, G' and G'', respectively; and the first and second normal stress differences, N_1 and N_2, respectively. We also present a study on the response of the emulsion's magnetization to the oscillatory strain for different external magnetic field conditions. In this investigation, we compute the magnetic susceptibility, χ, the angle between the magnetization and the external field, θ_{mag}, and the magnetic torque, $\boldsymbol{\tau}_{mag}$. These quantities are periodic under the oscillatory shear conditions, and were tracked by their in-phase and out-of-phase components relative to the strain.

All the analyses presented in this work are obtained for a cubic domain of side 8.125, with a mesh discretization of $104 \times 104 \times 104$ cells and a time step of $\Delta t = 4 \times 10^{-3}$. This domain size corresponds to a volume fraction of $\beta \approx 0.78\,\%$, characterizing a dilute emulsion, i.e. both magnetic and hydrodynamic interactions between the droplets are negligible. We set $\gamma_0 = Ca/\omega = 0.1$ and $Re = 10^{-3}$, so that the dimensionless strain amplitude is small and inertial effects are negligible, and the flow regime is compatible with the linear viscoelasticity limit. The magnetic permeability ratio is constant and set as $\zeta = 2$ throughout this work.

We evaluated the effects of time step, mesh refinement and domain size on the results in order to ensure convergence, considering the case of $\omega = 10$, $Ca = 1.0$ and $Ca_{mag} = 16$, for the magnetic field in the y-direction. In this analysis, we focused on the pair of rheological parameters (G', G''), which are directly related to the geometric parameters of the droplet. With $\Delta t = 1.0 \times 10^{-3}$ as the reference case, we found variations of $(0.413\,\%, 2.270\,\%)$ when increasing the time step to 4.0×10^{-3}, and $(0.978\,\%, 3.115\,\%)$ for $\Delta t = 8.0 \times 10^{-3}$. Regarding the mesh refinement, and considering a mesh of $208 \times 208 \times 208$ cells as the reference case, we observed relative variations of $(0.710\,\%, 0.738\,\%)$ for a mesh of $104 \times 104 \times 104$ cells, and $(0.896\,\%, 2.661\,\%)$ for a mesh of $64 \times 64 \times 64$ cells. Lastly, for the study of confinement effects, we focused on $(G'/\beta, G''/\beta)$ and found marginal variations of $(0.39\,\%, 0.46\,\%)$ when doubling the domain size from 8.125 to 16.25, while maintaining the same mesh refinement used throughout this work. Other parameters such as droplet deformation and inclination angle also displayed similarly negligible variations. Given the small variations observed for the tested time steps and mesh discretizations, and considering that these were run for the most critical values of ω and Ca_{mag} considered in this work, we can conclude that the chosen time step and mesh discretization have no considerable effects on the results presented in the following analyses. Based on the domain size study, we can also conclude that confinement effects are negligible.

4.1. *Verification*

The numerical methodology used in the present work is similar to that of Abicalil *et al.* (2021), and has been validated in the aforementioned work for the case of ferrofluid droplets in steady shear flows by comparisons with other results presented in the literature (Ishida & Matsunaga 2020). In order to verify the accuracy of the method for oscillatory shear flows, we provide a comparison with Palierne's analytical solution for dilute emulsions, which successfully describes the viscoelastic properties of a large variety of non-Newtonian fluids (Bousmina 1999; Boudoukhani, Moulai-Mostefa & Hammani 2020; Liao *et al.* 2020). To this end, we analyse the storage and loss moduli, G' and G'', for $0.1 \leqslant \omega \leqslant 10$ in the absence of magnetic fields. According to Palierne's model, the complex shear modulus for a homogeneous dilute emulsion is given by (Pal 2011)

$$G_e^*(\omega) = G_c^*(\omega) + 5\beta G_c^*(\omega)H^*(\omega), \tag{4.1}$$

where G_c^* is the complex shear modulus of the continuous phase, and the second term on the right-hand side accounts for the dispersed phase contribution. Under the assumptions that both phases are Newtonian and $\lambda = 1$, they share same complex shear modulus ωi, with $i = \sqrt{-1}$, and $H^*(\omega)$ reads

$$H^*(\omega) = \frac{28}{175G_c^*(\omega) + 80}. \tag{4.2}$$

Therefore, the contribution of the dispersed phase to the non-dimensional complex shear modulus of the emulsion is $28\beta G_c^*/(35G_c^* + 16)$. Recall that all terms presented here are in non-dimensional form according to the scales presented in § 2. To characterize the linear viscoelastic properties of our model, we use the classical Maxwell's approach in non-dimensional form, according to

$$S_{yx}(\omega, t) = G'(\omega)\frac{Ca}{\omega}\sin(\omega t) + G''(\omega)\frac{Ca}{\omega}\cos(\omega t), \tag{4.3}$$
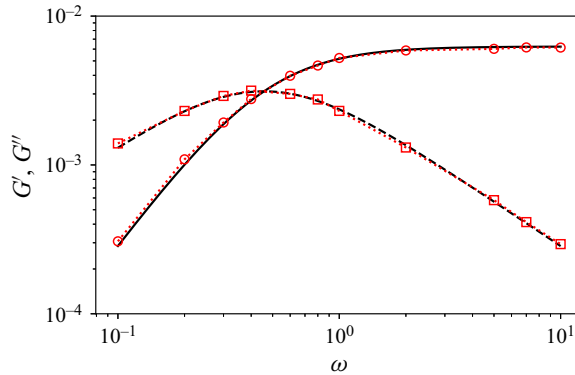
Figure 2. Elastic, G', and loss, G'', moduli as a function of the non-dimensional angular frequency, ω. Red circles and squares represent, respectively, our results for G' and G''. The solid and dashed black lines refer to Palierne's model (Palierne 1990).

where S_{yx} is the yx-component of the particle stress tensor $\boldsymbol{S}$ (Batchelor 1970), given by a surface integral over the droplet surface as (Cunha *et al.* 2020*b*; Abicalil *et al.* 2021)

$$\boldsymbol{S} = \frac{1}{V} \int_{\Gamma} \left[\boldsymbol{x} \left(\kappa - \frac{Ca_{mag}}{2}(\zeta - 1)H^2 \right) \hat{\boldsymbol{n}} \right] \mathrm{d}\Gamma. \tag{4.4}$$

Note that the particle stress tensor in (4.4) applies to non-steady regimes in the creeping flow limit, given that vorticity propagates instantaneously throughout the domain. In this way, any change in the boundary conditions is instantly perceived everywhere in the flow (Oliveira & Cunha 2015), such that (4.4) can be used to compute the particle stress in SAOS if the Stokes flow condition can be assumed in the droplet scale.

Due to the fact that G' and G'' decompose the time-dependent particle stress into an in-phase and an out-of-phase component with respect to the shear, it is possible to obtain both parameters by performing a fast Fourier transform on the periodic signal of S_{yx} over time.

Figure 2 compares our numerical results with Palierne's model for an emulsion composed of Newtonian fluids with the same viscosity and density. It can be seen that there is an overall excellent agreement between both models, indicating the accuracy of our methodology, including the use of Batchelor's particle stress approach. We also found that the crossing point between the curves for G' and G'' occurs at the frequency $\omega_{cp} = 0.45$, corresponding to a relaxation time of $t_d = 2.19$, which is in good agreement with the model reported by Graebling, Muller & Palierne (1993), where $t_d = 2.20$.

For $\omega < \omega_{cp}$, the emulsion behaves mostly as a viscous fluid. In this regime, the relaxation time is short in relation to the oscillation frequency, such that it has enough time to accommodate the changes in shear rate caused by the oscillatory flow. At the limit of $\omega \to 0$, the droplet approaches the steady-state condition for a simple shear flow of equal instant shear rate. Thus, for low oscillation frequencies, the droplet's response is primarily dependent on the instantaneous shear rate, such that $G' \ll G''$. On the other hand, for $\omega > \omega_{cp}$, the droplet's response is more dependent on the instantaneous shear strain, since the relaxation time is longer than the oscillation periods, resulting in $G' \gg G''$. For high-frequency values ($\omega > 2$), G' reaches a plateau region, with values approaching 0.006158.
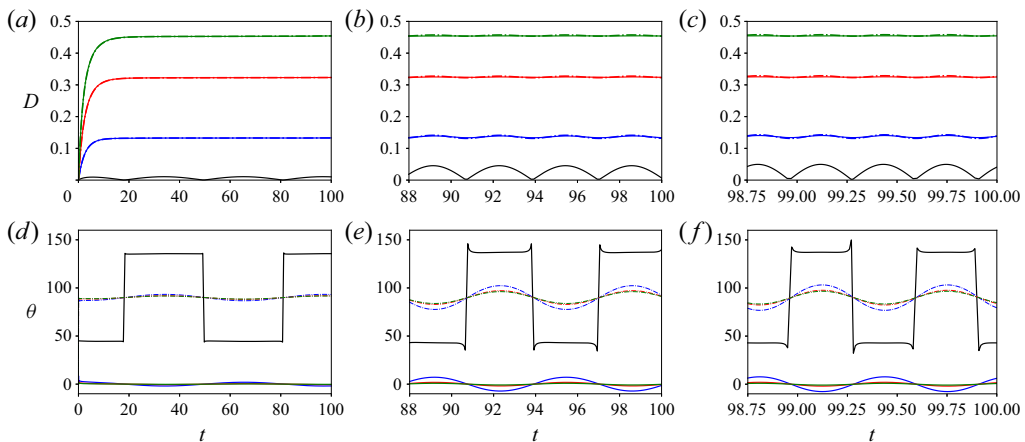
955 A3-10

Figure 3. Droplet's deformation, D, and inclination angle, θ, over time for the external magnetic field in the x (solid lines) and y-directions (dash-dotted lines) as a function of oscillatory shear frequency and Ca_{mag}. First column for $\omega = 0.10$, second for $\omega = 1.00$ and the last one for $\omega = 10.00$. Black lines represent the flow in the absence of magnetic field, blue lines refer to $Ca_{mag} = 4.00$, red to $Ca_{mag} = 10.00$ and green to $Ca_{mag} = 16.00$.

4.2. *Droplet geometrical properties*

In this subsection, we study the impact of the external magnetic field when applied in the x, y and z-directions on the droplet's deformation (D) and inclination angle (θ). These geometrical parameters were evaluated across several cycles, for $\omega = 0.10$, 1.00 and 10.00, representing regimes of low, intermediate, and high oscillation frequencies.

Figures 3 and 6 present the droplet's deformation and inclination over time for different cases, varying the magnetic field direction, oscillatory shear frequency and magnetic capillary number. First, we focus on the droplet dynamics in the absence of external magnetic fields. For $\omega = 0.10$, in figure 3(a), the droplet exhibits a deformation pattern following cyclic oscillations with a single mode, with frequency ω and amplitude of ≈ 0.01. Since the results presented in this work are for a constant oscillation amplitude, lower oscillation frequencies result in lower shear rates. In this case, the droplet barely deviates from the spherical shape. To understand the behaviour of the inclination angle in the oscillatory shear, it is instructive to recall that, under low capillary number regimes, the droplets incline up to $45°$ relative to the flow direction. In this manner, considering that for low frequencies and small strain amplitudes the instant ratio between shear stress and surface tension perceived by the droplet is compatible with a small capillary number, we conclude that θ must be close to either $45°$ or $135°$, depending only on the instant shear-rate direction. Keeping this in mind, the droplet's inclination oscillates like a binary wave (as illustrated in the movie in the supplementary material available at https:// doi.org/10.1017/jfm.2022.1019), sharply changing between $45°$ and $135°$ as displayed in figure 3(a).

Changing from $\omega = 0.10$ to 1.00, in figure 3(b), we observe a significant increase in the droplet's deformation amplitude, with the increased oscillation frequency resulting in higher characteristic Ca. Unlike the previous case, for $\omega = 1$ the shear stresses are comparable to the surface tension, allowing deformation peaks of $D \approx 0.045$. The binary behaviour of θ remained similar to the former case despite the slightly wider variations with $43° \lesssim \theta \lesssim 137°$. One can observe that, in this case, regardless of the higher shear rates imposed by ω, the short strain available for the droplet to deform prevents it from reaching even higher deformation values. Moreover, the increased shear rates also cause

the capillary forces to become progressively less significant. In this sense, we only observe modest variations for D and θ when increasing the frequency from $\omega = 1.00$ to 10.00 (figure 3c), when compared with the transition from $\omega = 0.10$ to 1.00. In this case, the peaks in D become ≈ 0.5, while the θ variations remained practically unchanged with respect to the case of $\omega = 1.00$. For high oscillation frequencies, the surface tension effects produced by the capillary forces eventually become negligible when compared with the large shear rates, such that the droplet's deformation becomes dependent solely on the applied strain, with peak deformations bounded by the strain amplitude.

The action of an external magnetic field on a ferrofluid droplet subjected to oscillatory shear changes the droplet's motion pattern, as illustrated in the movie in the supplementary material. For the external magnetic fields applied in the x and y-directions, as can be seen in figures 3(a), 3(b) and 3(c), the deformation behaviour is mostly insensitive to the field orientation and the shear frequency. Thus, even for the smallest relative magnetic field intensity considered, corresponding to $Ca_{mag} = 4.00$, the magnetic effects dominate the droplet's deformation. In this way, once the stationary regime is reached, there are only minimal oscillations in the droplet's deformation, even for high shear-rate frequencies. Interestingly, the amplitude of such oscillations is considerably smaller than in the cases with no external field. However, one can still notice that such variations are slightly larger for the field in the y-direction. In this case, as the field stretches the droplet to regions of faster flow, the droplet experiences a stronger effective shear, with the opposite effect occurring for fields applied in the x-direction (Cunha *et al.* 2018b; Abicalil *et al.* 2021). For $\omega = 10.00$ and magnetic fields in the y-direction, the deformation oscillates around $D = 0.1369 \pm 0.0059$ for $Ca_{mag} = 4.00$, $D = 0.3254 \pm 0.0034$ for $Ca_{mag} = 10.00$ and $D = 0.4553 \pm 0.0027$ for $Ca_{mag} = 16.00$, indicating a progressive action of the magnetic field in the sense of decreasing the amplitude of D oscillations.

Focusing on the droplet's inclination angle, in figures 3(d), 3(e) and 3(f), the capillary forces play no significant role when compared with the shear and magnetic effects, while the deformation and inclination amplitudes are bounded by the small strain amplitude, defined by γ_0 and constant across all cases. For $\omega = 0.10$, the droplet tends to accommodate in the magnetic field direction, presenting small oscillations for all cases of Ca_{mag}. Similar to the droplet's deformation when $\omega = 0.10$, the shear stresses are too weak to cause any significant changes in the droplet inclination. In any case, despite still being small, the amplitude of the inclination angle oscillations is greater for the magnetic field in the y-direction, since the droplet is subjected to stronger effective shear rates, and decreases with Ca_{mag}. For $Ca_{mag} = 4.00$, this amplitude is of $3.33°$ for the field in the y-direction, and of $1.96°$ for the field in the x-direction. For both $\omega = 1.00$ and 10.00, the droplet's inclination angle dynamics are pretty similar to each other. For the magnetic field in the x-direction with $Ca_{mag} = 10.00$ and 16.00, the magnetic effects overcome the shear forces, and the droplet stays mostly aligned to the field direction, presenting only weak oscillations, see figure 4(a). For $Ca_{mag} = 4.00$, such oscillations are more notable, presenting amplitudes of approximately $7.20°$ for both $\omega = 1.00$ and $\omega = 10.00$. The oscillations become more pronounced when the field is in the y-direction. The curves for the cases of $Ca_{mag} = 10.00$ and 16.00 mostly overlay each other, presenting amplitudes of approximately $6.16°$ for both $\omega = 1.00$ and $\omega = 10.00$, see figure 4(b). For $Ca_{mag} = 4.00$, we verify an oscillation amplitude of approximately $12.35°$ for both $\omega = 1.00$ and $\omega = 10.00$. The similarities between the results observed for $\omega = 1.00$ and 10.00 suggest a saturation of the droplet dynamics concerning the shear frequency. Such comprehension will be of great importance when studying the rheology of the present system in the following subsections.
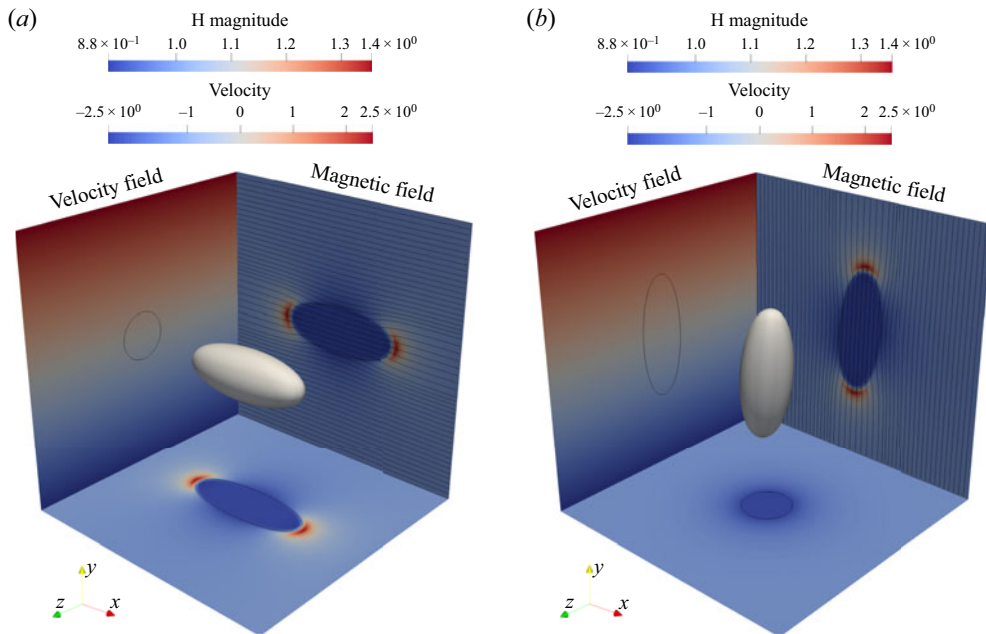
Figure 4. Oscillation amplitude for a droplet under an external magnetic field in the *x*-direction (*a*) and *y*-direction (*b*) for $Ca_{mag} = 16.00$ and $\omega = 10.00$. The droplet is projected into all orthogonal planes alongside the magnitude of the magnetic field in the *xz* and *xy*-planes, with the latter also containing the magnetic field lines. The *yz*-plane shows the velocity field.

The application of magnetic fields in the *z*-direction has different implications since the elongation of the droplet occurs perpendicularly to the shear plane. Figure 5(*a*) shows the droplet shape for different values of Ca_{mag}, from two perspectives. The primary consequence is that, in the *xy*-plane, the droplet's cross-section remains nearly circular. Additionally, as Ca_{mag} increases, this cross-sectional area decreases, in accordance with the conservation of the droplet's mass, given its elongation in the magnetic field direction.

The first key point to be analysed is the droplet's inclination angle in figures 6(*d*), 6(*e*) and 6(*f*). Given that the droplet presents a near-circular cross-section in the shear plane, similar to when there is no magnetic field, the droplet oscillates in a binary form regardless of Ca_{mag} and ω. It is possible to observe small spikes from the transition of one angle to the other, also present in the no-field case. These correspond to outliers, arising from the difficulty in determining the inclination angles as the cross-sections become smaller and circular (when the flow direction is reversing). Thus, such spikes are more pronounced for $Ca_{mag} = 16$.

For $\omega = 0.10$, it can be seen in figure 6(*a*) that smaller values of Ca_{mag} lead to higher deformation amplitudes, with $D \approx 0.011$ for $Ca_{mag} = 0$ (no magnetic field), and $D \approx 0.0081$ for $Ca_{mag} = 16$. For $\omega = 1.00$, figure 6(*b*) displays a similar dynamic, albeit with significantly larger deformation amplitudes, such as $D \approx 0.048$ for $Ca_{mag} = 0$ and $D \approx 0.043$ for $Ca_{mag} = 16$. In the case of $\omega = 10$, it can be seen in figure 6(*c*) that the curves collapse, becoming indistinguishable despite the different values of Ca_{mag}, with a deformation amplitude of $D \approx 0.051$. Figure 5(*b*) shows this phenomenon for $Ca_{mag} = 16$ and $\omega = 10$. We also expanded this study to $\omega = 12$ to check for a possible trend reversal and found that it only enhances the convergence of the curves. This result suggests that, for high oscillation frequencies, the influence of magnetic effects on the
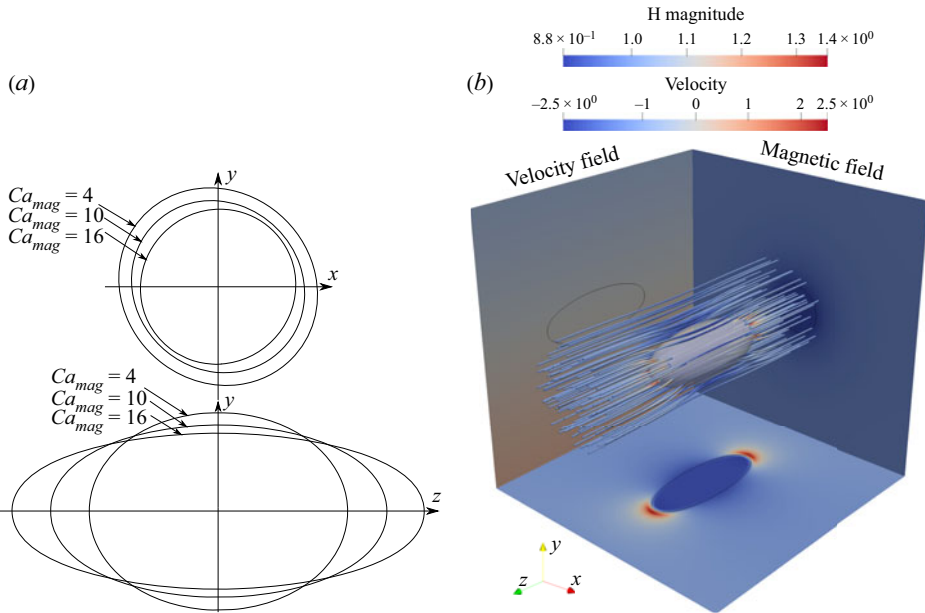
Figure 5. Panel (*a*) shows the droplet shape for the external magnetic field in the *z*-direction for $t = 91.64$, $\omega = 1.00$ and $Ca_{mag} = 4$, 10 and 16, as indicated by the legend. Panel (*b*) represents a three-dimensional view of the velocity (*yz*-plane) and magnetic field projections (*xz* and *xy*-planes) together with the magnetic streamlines around the droplet for $Ca_{mag} = 16$ and $\omega = 10$.
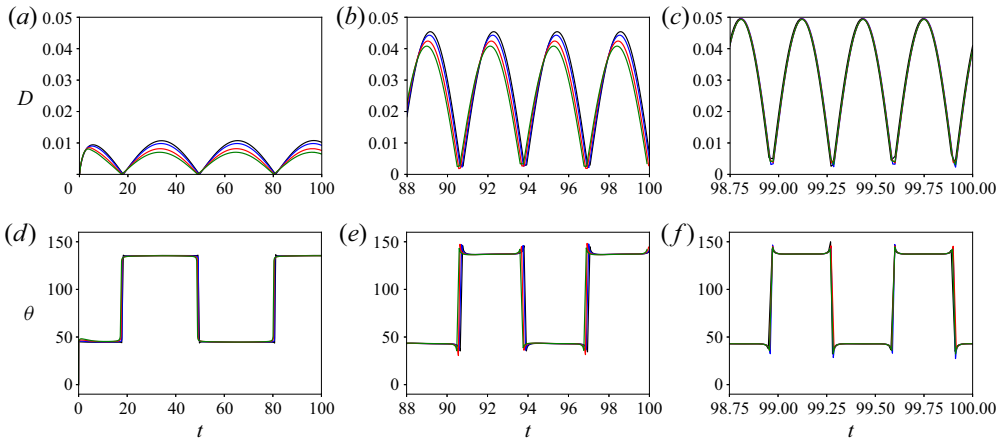

Figure 6. Droplet deformation, D, and inclination angle, θ, over time for the external magnetic field in the *z*-direction as a function of oscillatory shear frequency and Ca_{mag}. First column for $\omega = 0.10$, second for $\omega = 1.00$ and the last one for $\omega = 10.00$. Black lines represent the flow in the absence of magnetic field, blue lines refer to $Ca_{mag} = 4.00$, red to $Ca_{mag} = 10.00$ and green to $Ca_{mag} = 16.00$.

droplet's deformation becomes negligible. It is worth mentioning that this only applies to the droplet's deformation in the shear plane. The overall droplet shape is still dependent on the magnetic field intensity, with larger values of Ca_{mag} leading to larger droplet elongations in the field direction. It is interesting to note, especially in figure 6(*b*), that an increase in Ca_{mag} shifts both curves to the left. This dynamic may originate from the

955 A3-14

fact that the droplet decreases its radius in the shear plane, also decreasing its effective Ca and the relaxation times, as Ca_{mag} increases.

4.3. *Rheology of viscoelastic materials*

4.3.1. *Storage and loss shear moduli*

In this section, we investigate the influence of both the external magnetic fields, defined by the magnetic capillary number Ca_{mag} and the field direction, and the angular frequency ω on the emulsion's linear viscoelastic properties. As a consequence of the geometric dynamics reported in § 4.2, the droplet experiences changes in its storage and loss moduli.

The magnetic field in the x-direction acts reducing not only the droplet's oscillatory dynamics but also the effective shear effects. The primary consequence of the latter is a progressive decrease in the amplitude of the particle shear stress, S_{yx}, as Ca_{mag} increases. This behaviour can be observed through the in-phase (G') and out-of-phase (G'') components in figures 7(a) and 7(b). It can be seen that, despite the vertical displacements of the curves, the general behaviour as a function of angular frequency remains mostly unchanged and similar to the case in the absence of magnetic fields. For $\omega \to 0.1$, the long oscillation periods result in sufficient time for capillary effects to have a significant influence on the droplet's shape, in such a way that its deformation is mostly determined by the instant shear rate, resulting in $G' \ll G''$ and therefore in a mostly viscous behaviour. As the oscillation frequency increases, there is a gradual transition from this viscous to an elastic behaviour, with the point at which G' becomes greater than G'' occurring at $\omega_{cp} \approx 0.41$, regardless of magnetic capillary number. At high oscillation frequencies, the time required for the capillary effects to influence the droplet's shape becomes much larger than the oscillation periods, in such a way that capillary effects on the droplet's shape become negligible and, therefore, its deformation is governed by the instant shear strain. This results in $G' \gg G''$, and, thus, in the emulsion displaying a mostly elastic behaviour.

For external magnetic fields in the y-direction, an opposite effect is observed regarding changes in Ca_{mag}. As the magnetic capillary number increases, the droplet is elongated in the velocity gradient direction, therefore exposing it to a greater effective shear, and causing it to display larger variations of θ. In contrast to the case of magnetic fields in the x-direction, increases in Ca_{mag} result in larger amplitudes of S_{yx}, and therefore in increases of both the in-phase and out-of-phase components, as seen in figures 7(a) and 7(b). Similar to the case of magnetic fields in the x-direction, the droplet's response is predominantly dependent on the instantaneous shear rate at low oscillation frequencies, and on the shear strain at high frequencies. Despite the increase in viscoelastic components, the transition point in which G' becomes larger than G'' remains the same across the Ca_{mag} range, similar to what was observed for magnetic fields in the x-direction. Given that the percentage difference between the droplet relaxation time for the cases with and without the magnetic field is less than 9 %, we believe that the magnetic field does not change the droplet's effective relaxation time in both directions.

A different phenomenon happens when the magnetic field is in the z-direction. It can be seen, in figures 7(c) and 7(d), that there is a mixed behaviour, with different responses to variations in Ca_{mag} depending on the oscillation frequency. For low angular frequencies, with ω up to 0.1, both G' and G'' decrease with increasing Ca_{mag}, albeit in a much less pronounced form than what was observed for the other two directions cases, with changes in G'' mostly imperceptible. This is analogous to the behaviour in simple shear flows previously reported in the literature (Ishida & Matsunaga 2020; Abicalil *et al.* 2021). In contrast, for high oscillation frequencies ($\omega \to 10$), both G' and G'' increase with increasing Ca_{mag}.

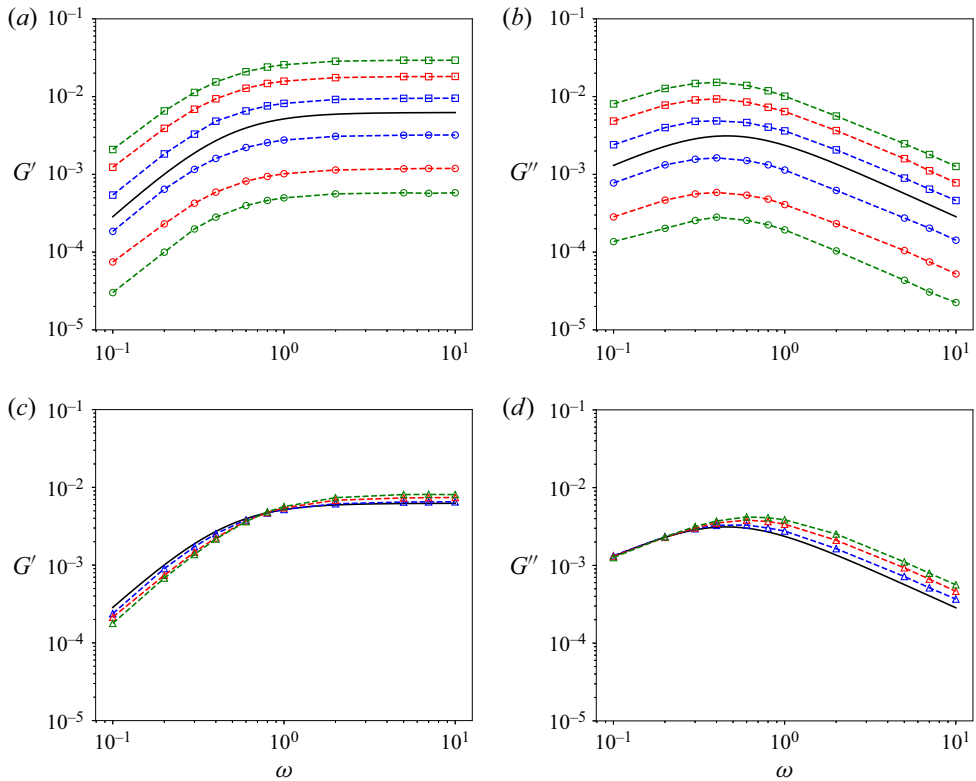Figure 7. Linear viscoelastic properties, G' and G'', for an external magnetic field in the x, y, and z directions. First column for G' and second one for G''. The first row represents the results for the x-direction (circle marks) and y-direction (squared marks). The second row shows the results for the z-direction (triangle marks). Black solid lines are for $Ca_{mag} = 0$ (Palierne 1990), blue lines are for $Ca_{mag} = 4$, red ones for $Ca_{mag} = 10$ and green ones for $Ca_{mag} = 16$

Figure 8 shows the same phenomenon by means of particle shear stress component S_{yx} for $\omega = 0.1$ (solid lines) and $\omega = 10$ (dashed lines). For $\omega = 0.1$, an increase in Ca_{mag} is associated with smaller amplitudes in the signal of S_{yx}, while the opposite is observed for $\omega = 10$. Alongside the data presented in figures 7(c) and 7(d), this leads to the conclusion that the decrease in amplitude of S_{yx} caused by larger magnetic capillary numbers at low oscillation frequencies is associated with the reduction in the viscoelastic properties. Conversely, the increase in the amplitude of S_{yx} with increases Ca_{mag} for high oscillation frequencies results in a greater interference of the droplet in the flow, resulting in the larger viscoelastic moduli.

It is interesting to note that, in contrast to what was observed for magnetic fields in the x- and y-directions, the presence of fields in the z-direction does lead to changes in the droplet's effective relaxation time. Based on the cross-over points in which G' becomes larger than G'', the droplet's effective relaxation time was measured to be of $t \approx 2.20$, 1.90, 1.62 and 1.45, for $Ca_{mag} = 0$, 4, 10 and 16, respectively. This is due to the reduction in the droplet's cross-sectional area, reported in §4.2 and in the previous paragraphs.

With regards to the changes observed in the viscoelastic moduli, these arise from changes in a balancing act between different effects. As the droplet is stretched in the
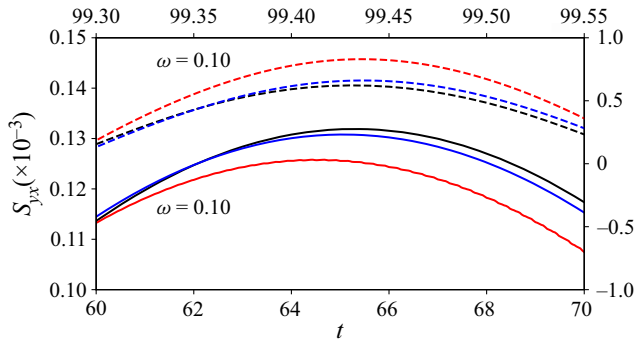
955 A3-16

Figure 8. The *yx* component of the particle stress given by (4.4) for $\omega = 10.00$ (dashed lines), relative to the top and right axes, and $\omega = 0.10$ (solid lines), relative to the bottom and left axes. Black, blue and red colours correspond to $Ca_{mag} = 0$, 4 and 16, respectively.

z-direction, its cross-sectional area is reduced, thereby subjecting it to a lower effective shear and reducing its influence on the flow at the central shear plane. However, the increase in length in the *z*-direction causes the droplet to interact with a larger fraction of shear planes – its frontal area relative to the flow direction is increased. For low oscillation frequencies, there is also an associated reduction in droplet's deformation, as discussed in §4.2. In this case, the balancing of these three effects leads to reductions in the viscoelastic moduli as Ca_{mag} increases, analogous to what is observed for simple shear flows (Abicalil *et al.* 2021). For high oscillation frequencies, however, the droplet's deformation becomes indifferent to changes in the magnetic capillary number, a fact that tips the balancing act between the three aforementioned effects in the opposite direction, resulting in the observed increases in both viscoelastic moduli with increasing magnetic capillary number.

4.3.2. *Normal stress difference*

As implicitly seen in §§4.2 and 4.3.1, the magnetic field produces higher stresses at the droplet tips than in the flattened regions. In this sense, we continue our discussion by analysing the droplet anisotropy by means of the first and second normal stress differences, respectively defined as $N_1 = S_{xx} - S_{yy}$ and $N_2 = S_{yy} - S_{zz}$.

Analysing (4.4), it is possible to see the influence of the magnetic field on the normal stress differences. At the droplet interface, while the magnetic field stretches the droplet in its direction, the surface tension tries to recover a spherical droplet shape. Furthermore, the term H^2 is maximized when the normal vector to the surface is aligned with the magnetic field. At this condition, the magnetic field tends to overcome the surface tension effects and N_1 (or N_2) may change signs.

Figure 9 presents N_1 and N_2 as a function of time for $\omega = 1.00$. Results for $\omega = 0.10$ and 10.00 are omitted due to their similarities with those of the presented case. In figure 9(*a*), the presence of magnetic fields in the *x*-direction results in $S_{xx} < S_{yy}$, an effect that is accentuated as Ca_{mag} increases, indicating the ability of the magnetic field to produce a preferential orientation and cause anisotropy. As Ca_{mag} increases, the oscillations in N_1 decrease, since the droplet barely diverges from the magnetic field orientation, as shown in §4.2. Since S_{yy} and S_{zz} are not significantly affected by the magnetic field, N_2 is largely independent of magnetic field intensity.

In figure 9(*b*), it can be seen that there is a symmetrical behaviour between N_1 and N_2, indicating that both S_{xx} and S_{zz} were not strongly affected by the magnetic field in the *y*-direction, i.e. the magnetic field only produced anisotropy in its respective direction.
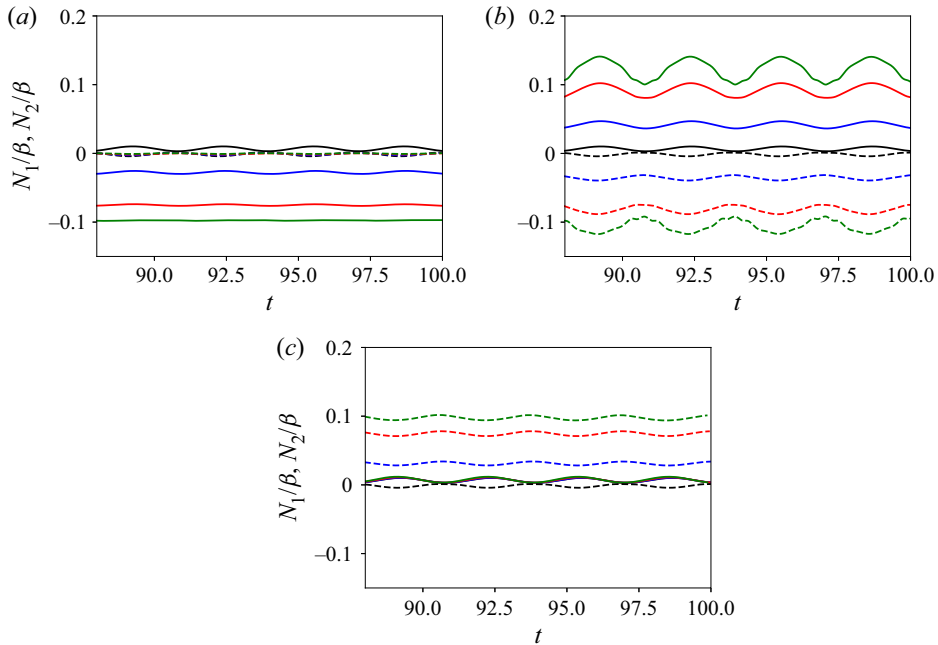
Figure 9. First (solid lines) and second (dashed lines) normal stress differences, scaled by the volume fraction, for an external magnetic field in the x (a), y (b) and z (c) directions and $\omega = 1.00$. Black, blue, red and green colours are, respectively, for $Ca_{mag} = 0$, 4, 10 and 16.

As seen in §§ 4.2 and 4.3.1, the presence of the droplet in a region of greater effective shear, as a function of Ca_{mag}, counterbalances the magnetic field effect. Consequently, the peaks of N_1 coincide with the lowest points of D, when the droplet is mostly aligned with the magnetic field; conversely, the valleys of N_1 coincide with the points of greatest deformation, where the droplet is least aligned with the magnetic field.

The third case is shown in figure 9(*c*), for external magnetic fields in the z-direction. In this case, N_1 is mostly unaffected by the presence of the magnetic field, since the anisotropies introduced by the field have no direct influence on S_{xx} and S_{yy}. Although values of N_1 for magnetic fields in the x-direction are mostly opposite and equal in magnitude to N_2 for the present case, the magnetic field in the z-direction does not restrict the droplet's orientation in the shear plane. Thus, the droplet's inclination angle changes with the oscillations in the shear flow, thereby leading to changes in S_{yy} as well and, in turn, to the oscillations observed in N_2.

These results indicate that external magnetic fields are capable of producing significant anisotropies in emulsions subjected to SAOS flows, similarly to what was previously reported for simple shear flows in two (Cunha *et al.* 2018*b*, 2020*b*) and three dimensions (Ishida & Matsunaga 2020; Abicalil *et al.* 2021). In summary, magnetic fields in the x-direction resulted in large negative values of N_1, with no significant changes in N_2; magnetic fields in the y-direction resulted in large positive values of N_1 and large negative values of N_2; and magnetic fields in the z-direction resulted in large positive values of N_2, with no significant changes in N_1.
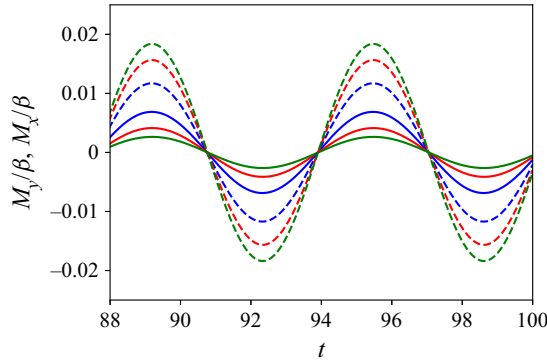
955 A3-18

Figure 10. Bulk magnetization scaled by the volume fraction for $\omega = 1.00$ and $Ca_{mag} = 4$ (blue lines), $Ca_{mag} = 10$ (red lines) and $Ca_{mag} = 16$ (green lines). Solid lines correspond to M_y for external magnetic fields in the x-direction, and dashed lines correspond to M_x for magnetic fields in the y-direction.

4.4. *Magnetization of dilute emulsion*

In this section, we investigate the magnetization of the emulsion, under the combined action of a SAOS flow and an external magnetic field. As reported by Abicalil *et al.* (2021) for the case of simple shear flows, despite the superparamagnetic behaviour of the droplet, there is a misalignment angle, θ_{mag}, between the bulk magnetization, $\langle M \rangle$, and the external field, H_0, which results in a magnetic torque, τ_{mag}.

4.4.1. *Magnetization*

We started this analysis by computing the non-dimensional bulk magnetization according to (Abicalil *et al.* 2021; Cunha *et al.* 2020*b*)

$$\langle M \rangle = \frac{1}{V} \int_V (\zeta_\epsilon(\phi) - 1) H \, dV, \tag{4.5}$$

where the magnetization effects are restricted to the droplet, since $\zeta_\epsilon(\phi) = 1$ in the continuous phase.

As seen in § 4.2, when the magnetic field is in the x-direction, the droplet remains elongated with D approximately constant. Among the three components of the vector $\langle M \rangle$, only M_y displays a periodic oscillation over time. Analogously, for magnetic fields oriented in the y-direction, only the x component of $\langle M \rangle$ oscillates. For external magnetic fields in the z-direction the magnetization does not oscillate.

Figure 10 presents the y component of the bulk magnetization for magnetic fields in the x-direction (solid lines), as well as the x component of the bulk magnetization for magnetic fields in the y-direction (dashed lines), for $\omega = 1.00$. For external magnetic fields in the x-direction, the droplet is confined in a region of weaker effective shear and stays approximately aligned with the magnetic field, as shown in § 4.2. Since the amplitude of θ decreases as Ca_{mag} increases, the amplitude of M_y decreases as well, even though the average values of $|\langle M \rangle|/\beta$ increase. Specifically, we have the average values of $|\langle M \rangle|/\beta = 0.8$, 0.86 and 0.89, while M_y/β reaches peaks of 0.006, 0.004 and 0.003, for $Ca_{mag} = 4$, 10 and 16, respectively. Thus, M_y has little influence on the signal of $\langle M \rangle$, which remains approximately a straight line. In the case of external magnetic fields in the y-direction, the average values of $|\langle M \rangle|/\beta$ increase in a similar way and approximately with the same values as for the case of magnetic fields in the x-direction. However, it can be seen that the magnetization amplitude increases with increasing Ca_{mag},
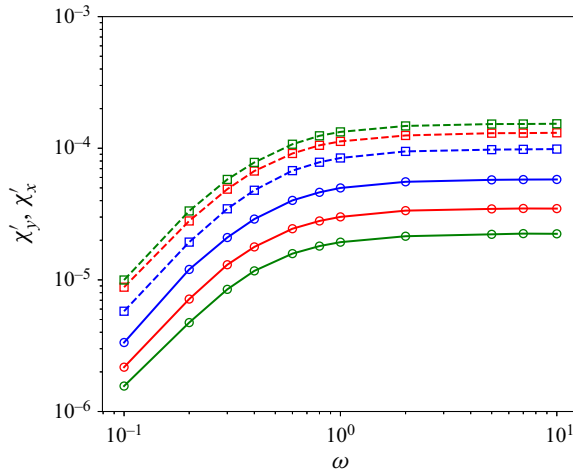
Figure 11. In-phase component of the bulk magnetization, χ', as a function of angular frequency for $Ca_{mag} = 4$ (blue lines), $Ca_{mag} = 10$ (red lines) and $Ca_{mag} = 16$ (green lines). Solid lines represent χ'_y for the magnetic field in the x-direction and dashed lines χ'_x for the magnetic field in the y-direction.

presenting peaks of $M_x/\beta = 0.012$, 0.016 and 0.018 for $Ca_{mag} = 4$, 10 and 16, respectively. In this case, even though the amplitude of the droplet's inclination angle also reduces with increasing Ca_{mag}, this reduction is far less significant than for the case of external magnetic fields in the x-direction, in such a way that the increase in the droplet's deformation associated with higher values of Ca_{mag} end up leading to increases in the amplitude of M_x. Similarly, M_x has little influence on the signal of $\langle M \rangle$, which remains approximately constant.

The magnetization signal can be analysed following a similar methodology to that employed in § 4.3.1 for the particle shear stress. In this way, we have that

$$M_k = \chi'_k \sin \omega t + \chi''_k \cos \omega t, \tag{4.6}$$

where k designates the magnetization component. The component χ'_k is in phase with the shear strain and the component χ''_k is 90° out of phase, i.e. in phase with the shear rate.

Figures 11 and 12 present both the in-phase and out-of-phase components based on (4.6). The first point to be discussed is the similarity with the viscoelastic properties in § 4.3.1. No significant differences in M_k were observed for $\omega \gtrsim 1$, indicating a saturation plateau as a function of Ca_{mag}. We also found a non-zero χ'', indicating that the periodic response of $\langle M \rangle$ has an out-of-phase component in relation to the imposed periodic shear. That means the magnetization displays a finite relaxation time, associated with the emulsions' mechanical response to the periodic shear. The frequency in which χ' and χ'' are equal is $\omega = 0.41$, which is precisely the same frequency in which $G' = G''$. That is a strong indication that the mechanism of magnetization relaxation in dilute magnetic emulsions originates from the periodic variations of the droplet shape and orientation in the micro-scale (the same mechanism originating the mechanical viscoelastic response). In this sense, the effective magnetic susceptibility, based on the periodic components and given by $\chi = \sqrt{\chi'^2 + \chi''^2}$, is higher for high oscillation frequencies (with the emulsion displaying a solid-like behaviour) than for lower oscillation frequencies (with the emulsion displaying a liquid-like behaviour).
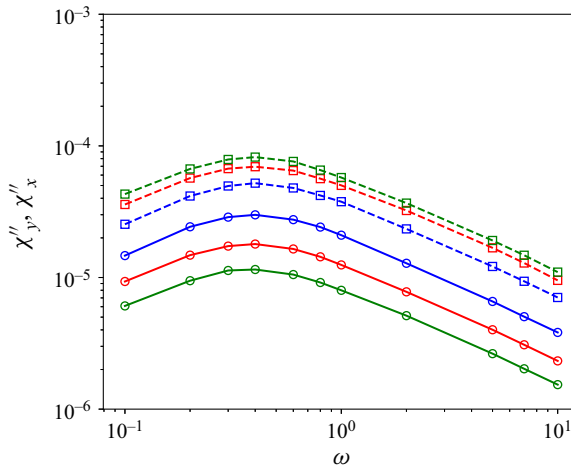
955 A3-20

Figure 12. Out-of-phase component of the bulk magnetization, χ'', as a function of angular frequency for $Ca_{mag} = 4$ (blue lines), $Ca_{mag} = 10$ (red lines) and $Ca_{mag} = 16$ (green lines). Solid lines represent χ''_y for the magnetic field in the x-direction and dashed lines χ''_x for the magnetic field in the y-direction.

It is worth mentioning that, for some of the high values of Ca_{mag} ($\gtrsim 10$) explored in this work, it is likely that ordinary ferrofluids would reach nonlinear regimes of magnetization. To achieve such high Ca_{mag} values and still maintain the linear regime in experiments with currently feasible ferrofluids, one would need to drastically reduce the interfacial tension to something of the order of 10^{-3} N m^{-1} by the use of surfactants, and prepare emulsion samples with millimetre-sized droplets.

4.4.2. *Angle between $\langle M \rangle$ and H_0*

Under the combined action of the shear flow and the external magnetic field, M and H_0 are not aligned, even for a superparamagnetic droplet. The angle, θ_{mag}, between M and H_0, depends on the droplet's deformation, external magnetic field intensity, and the external magnetic field direction.

Figure 13 shows θ_{mag} for $\omega = 1.00$. In this case, θ_{mag} has a direct relationship with the previously analysed magnetization components. Both M_x and M_y are used to express this parameter, i.e. $\theta_{mag} = \sin^{-1}(M_y/|\langle M \rangle|)$ and $\theta_{mag} = \sin^{-1}(M_x/|\langle M \rangle|)$ for magnetic fields in the x and y-directions, respectively. Thus, as the magnetic field in the x-direction confines the droplet, and consequently the magnetization vector, θ_{mag} oscillations decrease with increasing Ca_{mag}, with amplitudes of $\theta_{mag} \approx 0.48, 0.28$ and 0.17 for $Ca_{mag} = 4, 10$ and 16, respectively. In contrast, with the magnetic field oriented in the y-direction, the amplitudes tend to increase with Ca_{mag}, as the droplet experiences higher effective shear rates and thus relatively smaller reductions in inclination angle oscillations. Specifically, the amplitudes are of $\theta_{mag} \approx 0.83, 1.04$ and 1.17 for $Ca_{mag} = 4, 10$ and 16, respectively.

The angle θ_{mag} can also be analysed similarly to the stress and susceptibility, using the equation

$$\theta_{mag} = \theta'_{mag} \sin \omega t + \theta''_{mag} \cos \omega t, \tag{4.7}$$

to decompose θ_{mag} into components in phase (θ'_{mag}) and out of phase (θ''_{mag}) with the shear rate.
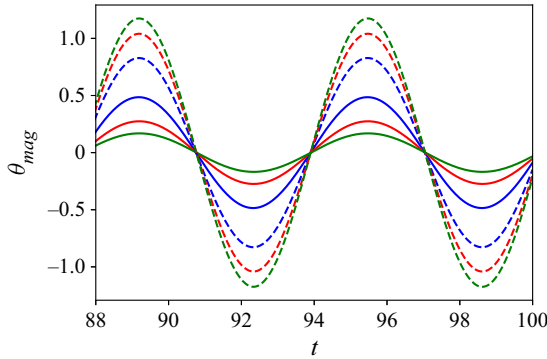
Figure 13. Angle between $\langle \boldsymbol{M} \rangle$ and $\boldsymbol{H}_0$, θ_{mag}, in degrees, for an external magnetic field in the x (solid lines) and y-directions (dashed lines), for $Ca_{mag} = 4$ (blue lines), $Ca_{mag} = 10$ (red lines) and $Ca_{mag} = 16$ (green lines).
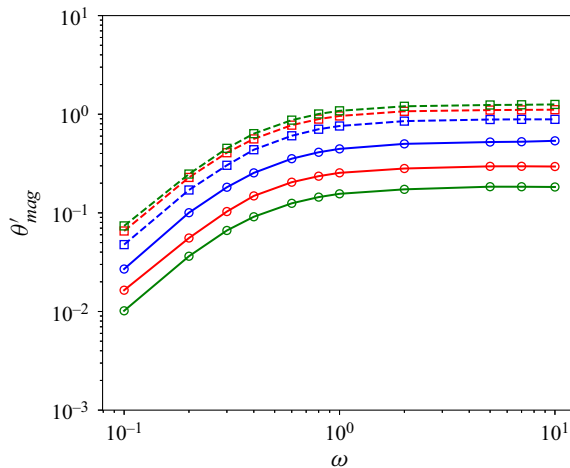

Figure 14. In-phase component of θ_{mag}, θ', as a function of angular frequency for $Ca_{mag} = 4$ (blue lines), $Ca_{mag} = 10$ (red lines) and $Ca_{mag} = 16$ (green lines). Solid lines correspond to magnetic fields in the x-direction, and dashed lines correspond to magnetic fields in the y-direction.

Since θ_{mag} is calculated as a function of the magnetization components, the results are entirely similar to those of the magnetization, including the cross-over point, as can be seen in figures 14 and 15. It is worth mentioning that, although the equation of θ_{mag} expresses a nonlinear relation to $\langle \boldsymbol{M} \rangle$, for small arguments we can rewrite it as $\theta_{mag} = M_y/|\langle \boldsymbol{M} \rangle|$ and $\theta_{mag} = M_x/|\langle \boldsymbol{M} \rangle|$.

4.4.3. *Magnetic torque*

A magnetic torque in the fluid arises because $\boldsymbol{M}$ and $\boldsymbol{H}_0$ are not perfectly aligned. This magnetic torque is counteracted by an opposing hydrodynamic torque, ensuring the conservation of angular momentum (Cunha *et al.* 2020b; Abicalil *et al.* 2021). This induced hydrodynamic torque manifests itself as asymmetries in the particle stress tensor, described in (4.4). In our study, we compute the non-dimensional magnetic torque, $\boldsymbol{\tau}_{mag}$, normalized by σ/a, using the following expression (Rosensweig 2013; Cunha *et al.* 2020b;
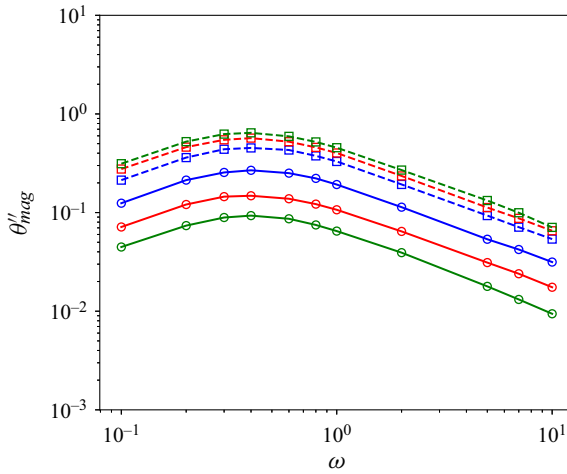
Figure 15. Out-of-phase component of θ_{mag}, θ'', as a function of angular frequency for $Ca_{mag} = 4$ (blue lines), $Ca_{mag} = 10$ (red lines) and $Ca_{mag} = 16$ (green lines). Solid lines correspond to magnetic fields in the x-direction, and dashed lines correspond to magnetic fields in the y-direction.
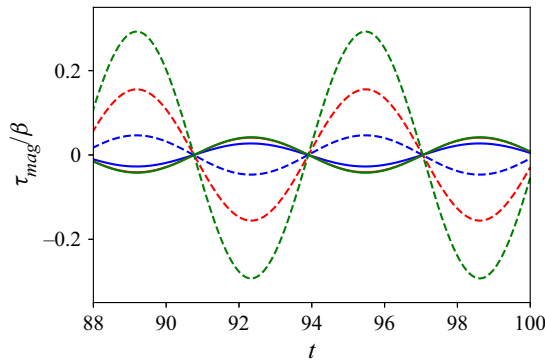

Figure 16. Torque scaled by σ/a for external magnetic fields in the x (solid lines) and y-directions (dashed lines), with $Ca_{mag} = 4$ (blue lines), $Ca_{mag} = 10$ (red lines) and $Ca_{mag} = 16$ (green lines).

Abicalil *et al.* 2021)

$$\boldsymbol{\tau}_{mag} = Ca_{mag} \langle \boldsymbol{M} \rangle \times \boldsymbol{H}_0, \tag{4.8}$$

highlighting that $\boldsymbol{\tau}_{mag}$ is proportional to both $|\langle \boldsymbol{M} \rangle|$ and $\sin \theta_{mag}$ (Abicalil *et al.* 2021).

Figure 16 presents the magnetic torque magnitude, τ_{mag}, scaled by β over time for the magnetic field in the x (solid lines) and y-directions (dashed lines). It can be seen that the peaks of magnetic torque for magnetic fields in the x-direction correspond to the valleys for fields in the y-direction, i.e. they act in opposite directions. As shown in figures 3 and 4, during the first half of its oscillation cycle, the droplet always assumes inclination angles in the range $0° < \theta < 90°$, regardless of magnetic field direction. Since the magnetic torque acts in the direction of aligning the droplet to the magnetic field, this results in a clockwise torque for magnetic fields in the x-direction, and counter-clockwise torques for magnetic fields in the y-direction. For the second half of the oscillation cycle, both torques act in opposite directions.
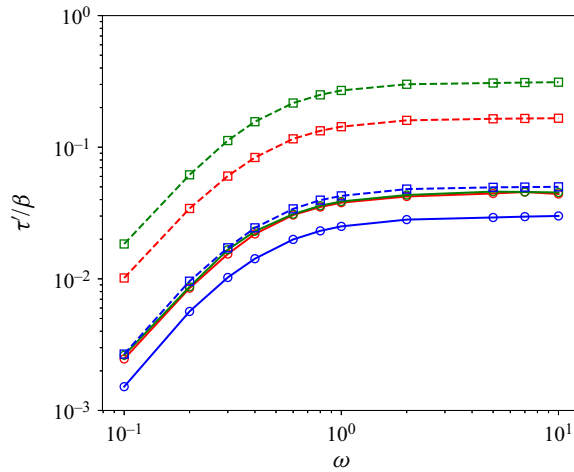
Figure 17. In-phase, τ', component of the torque scale by $\sigma\beta/a$ as a function of angular frequency for $Ca_{mag} = 4$ (blue lines), $Ca_{mag} = 10$ (red lines) and $Ca_{mag} = 16$ (green lines). Solid lines are for the magnetic field in the x-direction and dashed lines are for the magnetic field in the y-direction.

It can also be seen in figure 16 that, for magnetic fields in the x-direction, increasing Ca_{mag} from 4 to 10 leads to an increase in torque amplitude, with the increase in magnetization magnitude overcoming the reduction in the angle between $\langle M \rangle$ and H_0. However, further increasing in Ca_{mag} to 16 does not significantly change the torque amplitude, due to the increase in magnetization and reduction in θ_{mag} balancing each other out. For external magnetic fields in the y-direction, increases in Ca_{mag} lead to increases in both magnetization and θ_{mag}, and therefore also to increases in torque amplitude.

Focusing on the signal of the non-dimensional magnetic torque, it can be decomposed using the definition

$$\frac{\tau_{mag}}{\beta} = \alpha \left[\frac{\tau'}{\beta} \sin \omega t + \frac{\tau''}{\beta} \cos \omega t \right], \tag{4.9}$$

where τ' and τ'' are the in-phase and out-of-phase components with the strain, also normalized by σ/a. As seen in figure 16, the magnetic field in the x-direction produces a π rad phase shift in relation to the y-direction, which implies negative amplitudes in the decomposition. Therefore, in order to compare the in-phase and out-of-phase components for both magnetic field orientations, we adopt $\alpha = -1$ when the magnetic field is in x-direction and $\alpha = 1$ for magnetic fields in the y-direction.

Both of the aforementioned torque components are presented in figures 17 and 18. It can be seen that the overall behaviour, as a function of angular frequency, is similar to those observed for the magnetization components and θ_{mag}, including the cross-over point at the same oscillation frequency. Note that there is a progressive increase for the in-phase component in the plateau region, with torques for the magnetic field in the x-direction of approximately 0.03, 0.044 and 0.046 for $Ca_{mag} = 4$, 10 and 16, respectively. In this context, it is possible to see that the increment from $Ca_{mag} = 10$ to 16 is not significant, as the decrease in values of θ_{mag} balances the increase in magnetization magnitude. For the magnetic field in y-direction, the plateau region corresponds to torques of approximately 0.05, 0.17 and 0.31 for $Ca_{mag} = 4$, 10 and 16, respectively. Interestingly, the curves for $Ca_{mag} = 16$ and magnetic fields in the x-direction are nearly equal to those for $Ca_{mag} = 4$ and magnetic fields in the y-direction.
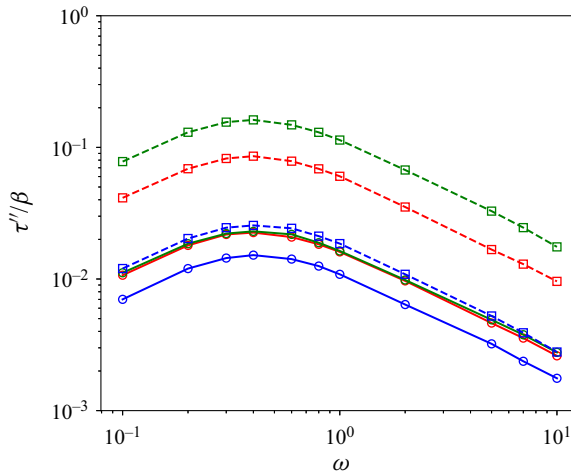
955 A3-24

Figure 18. Out-of-phase, τ'', component of the torque scale by $\sigma\beta/a$ as a function of angular frequency for $Ca_{mag} = 4$ (blue lines), $Ca_{mag} = 10$ (red lines) and $Ca_{mag} = 16$ (green lines). Solid lines are for the magnetic field in the x-direction and dashed lines are for the magnetic field in the y-direction.

5. Concluding remarks

The present study reported a three-dimensional computational analysis of a magnetic droplet suspended in non-magnetic matrix fluid, characterizing a dilute ferrofluid emulsion, subjected to a SAOS flow and an external magnetic field. The domain was discretized through the finite-difference method, using the level-set method for interface capturing and a semi-implicit projection method to solve the Navier–Stokes equations.

We evaluated the behaviour of the droplet as a function of the magnetic field orientation, angular frequency, and the intensity of the magnetic field. In order to ensure a linear regime of droplet dynamics and avoid the appearance of any higher harmonics, we set the strain amplitude to $\gamma_0 = 0.1$, constituting a SAOS flow. Based on these assumptions, it was possible to evaluate the morphological, rheological and magnetization behaviours of the emulsion, such as the droplet geometry, viscoelastic properties, normal stress differences and magnetization characteristics such as bulk magnetization, the angle between $\langle M \rangle$ and H_0 and the magnetic torque.

With regards to the emulsion's morphology, we found that droplet deformation is mostly insensitive to the direction of the magnetic field, if it is either the x or y-directions, with increasing Ca_{mag} leading to increases in droplet deformation. The behaviour of the droplet's inclination angle, meanwhile, did vary significantly depending on the magnetic field direction. For magnetic fields in the x-direction, the droplet is confined to regions of lower effective shear, attenuating the flow's effects on the droplet and reducing the inclination angle amplitude. For magnetic fields in the y-direction, the droplet is stretched alongside the main velocity gradient, subjecting it to a higher effective shear, and resulting in larger inclination angle amplitudes. In both cases, increases in magnetic capillary number reduce the inclination angle amplitudes.

A new phenomenon was observed when the magnetic field was in the z-direction. In this case, the droplet is elongated in the direction perpendicular to the shear plane, remaining nearly circular in the shear plane and consequently not significantly altering the oscillations of θ. However, this effect results in a decrease in the effective relaxation time

of the droplet, causing the deformation curves to converge into one for high oscillation frequencies, despite higher magnetic capillary numbers leading to lower deformations for low oscillation frequencies.

Based on this geometric dynamics, the viscoelastic properties are then a direct consequence of these behaviours. For magnetic fields in the x and y-directions, the emulsion displayed a mostly viscous behaviour for low frequencies, with $G'' \ll G'$. For high oscillation frequencies, G' reached a plateau region, with $G' \gg G''$, the typical behaviour of a Hookean solid, i.e. a mostly elastic behaviour. In addition, no significant differences in the cross-over point between G' and G'' were found, suggesting that the droplet's effective relaxation time is insensitive to both the x and y magnetic fields. Despite these similarities, the magnetic field in the x-direction decreases the magnitude of both viscoelastic components as Ca_{mag} increases, a direct consequence of the confining effects the magnetic field has on the droplet. In the y-direction, given that the magnetic field projects the droplet into a region of higher effective shear rate, both viscoelastic components increase with Ca_{mag}. For magnetic fields in the z-direction, there is a balance between the influence of the droplet area in the shear plane and its projected area in the flow. At low oscillation frequencies, the smaller deformations result in a decrease in both viscoelastic components with increasing Ca_{mag}. Meanwhile, at high oscillation frequencies, the convergence of the droplet deformations result in increases in Ca_{mag} leading to increases in both viscoelastic moduli, a behaviour opposite to the one displayed for low frequencies.

Regarding the normal stress differences, we found that the anisotropies produced by the magnetic field depend only on its strength and direction.

The magnetization properties are a direct consequence of the droplet dynamics. In the x-direction, the magnetic field leads the droplet to confinement effects that, although increasing the bulk magnetization as Ca_{mag} increases, reduce the effects on the periodic component of the bulk magnetization vector, and consequently, θ_{mag}. Given that the increase in bulk magnetization overcomes the reduction in θ_{mag}, there is the presence of a magnetic torque, in the sense of aligning the droplet to the magnetic field, that increases with Ca_{mag}. In the y-direction, as the magnetic field increases in strength, the droplet is elongated to a region of higher effective shear rate, increasing the magnitude of the bulk magnetization, the periodic component of the magnetization vector and, therefore, the angle between $\langle M \rangle$ and H_0. Consequently, there is the presence of an increasing magnetic torque with increases in Ca_{mag}. It is essential to mention that the cross-over point of all these properties was the same, revealing a deep dependence of $\langle M \rangle$, θ_{mag} and τ_{mag} on the interfacial characteristics of the droplet. Furthermore, despite the droplet being superparamagnetic, its interfacial dynamics causes it to display a finite magnetization relaxation time.

Author ORCIDs.

Ⓑ Rodrigo F. Abdo https://orcid.org/0000-0002-7232-4704;

Ⓑ Victor G. Abicalil https://orcid.org/0000-0001-6081-3984;

Lucas H.P. Cunha https://orcid.org/0000-0001-9613-0659;

Taygoara F. Oliveira https://orcid.org/0000-0003-2957-537X.

REFERENCES

ABICALIL, V.G.E., ABDO, R.F., DA CUNHA, L.H.P. & DE OLIVEIRA, T.F. 2021 On the magnetization of dilute ferrofluid emulsions in shear flows. *Phys. Fluids* **33** (5), 053313.

BADALASSI, V.E., CENICEROS, H.D. & BANERJEE, S. 2003 Computation of multiphase systems with phase field models. *J. Comput. Phys.* **190** (2), 371–397.

BAI, L., HUAN, S., ROJAS, O.J. & MCCLEMENTS, D.J. 2021 Recent innovations in emulsion science and technology for food applications. *J. Agr. Food Chem.* **69** (32), 8944–8963.

BATCHELOR, G.K. 1970 The stress system in a suspension of force-free particles. *J. Fluid Mech.* **41** (3), 545–570.

BHATIA, H., NORGARD, G., PASCUCCI, V. & BREMER, P. 2013 The Helmholtz–Hodge decomposition—a survey. *IEEE Trans. Vis. Comput. Graphics* **19** (8), 1386–1404.

BIJARCHI, M.A., DIZANI, M., HONARMAND, M. & SHAFII, M.B. 2021 Splitting dynamics of ferrofluid droplets inside a microfluidic T-junction using a pulse-width modulated magnetic field in micro-magnetofluidics. *Soft Matt.* **17** (5), 1317–1329.

BIJARCHI, M.A., FAVAKEH, A., SEDIGHI, E. & SHAFII, M.B. 2020 Ferrofluid droplet manipulation using an adjustable alternating magnetic field. *Sensors Actuators* **301**, 111753.

BOUDOUKHANI, M., MOULAI-MOSTEFA, N. & HAMMANI, S. 2020 Prediction of rheological properties and interfacial tension of mixtures of immiscible polypropylene-polystyrene (pp3/ps) blends. *Walailak J. Sci. Technol. (WJST)* **17** (7), 665–677.

BOUSMINA, M. 1999 Rheology of polymer blends: linear model for viscoelastic emulsions. *Rheol. Acta* **38**, 73–83.

CAPOBIANCHI, P., LAPPA, M., OLIVEIRA, M.S.N. & PINHO, F.T. 2021 Shear rheology of a dilute emulsion of ferrofluid droplets dispersed in a nonmagnetizable carrier fluid under the influence of a uniform magnetic field. *J. Rheol.* **65** (5), 925–941.

CAVALLO, R., GUIDO, S. & SIMEONE, M. 2003 Drop deformation under small-amplitude oscillatory shear flow. *Rheol. Acta* **42** (1), 1–9.

CHEN, D., YANG, Z., JI, Y., DAI, Y., FENG, L. & ARAI, F. 2021 Deformable ferrofluid-based millirobot with high motion accuracy and high output force. *Appl. Phys. Lett.* **118** (13), 134101.

CHORIN, A.J. 1968 Numerical solution of the Navier–Stokes equations. *Maths Comput.* **22** (104), 745–762.

COSTA, P. 2018 A FFT-based finite-difference solver for massively-parallel direct numerical simulations of turbulent flows. *Comput. Maths Applics.* **76** (8), 1853–1862.

CUNHA, F.R. & ROSA, A.P. 2021 Effect of particle dipolar interactions on the viscoelastic response of dilute ferrofluids undergoing oscillatory shear. *Phys. Fluids* **33** (9), 092004.

CUNHA, L.H.P., SIQUEIRA, I.R., ALBUQUERQUE, E.L. & OLIVEIRA, T.F. 2018*a* Flow of emulsion drops through a constricted microcapillary channel. *Intl J. Multiphase Flow* **103**, 141–150.

CUNHA, L.H.P., SIQUEIRA, I.R., CAMPOS, A.A.R., ROSA, A.P. & OLIVEIRA, T.F. 2020*a* A numerical study on heat transfer of a ferrofluid flow in a square cavity under simultaneous gravitational and magnetic convection. *Theor. Comput. Fluid Dyn.* **34** (1), 119–132.

CUNHA, L.H.P., SIQUEIRA, I.R., CUNHA, F.R. & OLIVEIRA, T.F. 2020*b* Effects of external magnetic fields on the rheology and magnetization of dilute emulsions of ferrofluid droplets in shear flows. *Phys. Fluids* **32** (7), 073306.

CUNHA, L.H.P., SIQUEIRA, I.R., OLIVEIRA, T.F. & CENICEROS, H.D. 2018*b* Field-induced control of ferrofluid emulsion rheology and droplet break-up in shear flows. *Phys. Fluids* **30** (12), 122110.

DE SIQUEIRA, I.R., REBOUÇAS, R.B., DA CUNHA, L.H.P. & DE OLIVEIRA, T.F. 2018 On the volume conservation of emulsion drops in boundary integral simulations. *J. Braz. Soc. Mech. Sci. Engng* **40** (1), 3.

DIERKING, I., YOSHIDA, S., KELLY, T. & PITCHER, W. 2020 Liquid crystal–ferrofluid emulsions. *Soft Matt.* **16** (26), 6021–6031.

DODD, M.S. & FERRANTE, A. 2014 A fast pressure-correction method for incompressible two-fluid flows. *J. Comput. Phys.* **273**, 416–434.

FAN, X., DONG, X., KARACAKOL, A.C., XIE, H. & SITTI, M. 2020*a* Reconfigurable multifunctional ferrofluid droplet robots. *Proc. Natl Acad. Sci. USA* **117** (45), 27916–27926.

FAN, X., SUN, M., SUN, L. & XIE, H. 2020*b* Ferrofluid droplets as liquid microrobots with multiple deformabilities. *Adv. Funct. Mater.* **30** (24), 2000138.

FRÖHLICH, A. & SACK, R. 1946 Theory of the rheological properties of dispersions. *Proc. R. Soc. Lond.* A **185** (1003), 415–430.

GHIGLIOTTI, G., BIBEN, T. & MISBAH, C. 2010 Rheology of a dilute two-dimensional suspension of vesicles. *J. Fluid Mech.* **653**, 489–518.

GIBOU, F., FEDKIW, R. & OSHER, S. 2018 A review of level-set methods and some recent applications. *J. Comput. Phys.* **353**, 82–109.

GOTTLIEB, S., KETCHESON, D.I. & SHU, C.-W. 2011 *Strong Stability Preserving Runge–Kutta and Multistep Time Discretizations*. World Scientific.

GRAEBLING, D., MULLER, R. & PALIERNE, J.F. 1993 Linear viscoelastic behavior of some incompatible polymer blends in the melt. Interpretation of data with a model of emulsion of viscoelastic liquids. *Macromolecules* **26** (2), 320–329.

GUIDO, C.J. & SHAQFEH, E.S.G. 2019 The rheology of soft bodies suspended in the simple shear flow of a viscoelastic fluid. *J. Non-Newtonian Fluid Mech.* **273**, 104183.

GUIDO, S., GROSSO, M. & MAFFETTONE, P.L. 2004 Newtonian drop in a Newtonian matrix subjected to large amplitude oscillatory shear flows. *Rheol. Acta* **43** (6), 575–583.

HARLOW, F.H. & WELCH, J.E. 1965 Numerical calculation of time-dependent viscous incompressible flow of fluid with free surface. *Phys. Fluids* **8** (12), 2182–2189.

HASSAN, MD.R. & WANG, C. 2019 Magnetic field induced ferrofluid droplet breakup in a simple shear flow at a low Reynolds number. *Phys. Fluids* **31** (12), 127104.

HASSAN, MD.R., ZHANG, J. & WANG, C. 2018 Deformation of a ferrofluid droplet in simple shear flows under uniform magnetic fields. *Phys. Fluids* **30** (9), 092002.

IOANNOU, N., LIU, H. & ZHANG, Y.H. 2016 Droplet dynamics in confinement. *J. Comput. Sci.* **17**, 463–474.

ISHIDA, S. & MATSUNAGA, D. 2020 Rheology of a dilute ferrofluid droplet suspension in shear flow: viscosity and normal stress differences. *Phys. Rev. Fluids* **5**, 123603.

ISHIDA, S., YANG, Y., MENG, F. & MATSUNAGA, D. 2022 Field-controlling patterns of sheared ferrofluid droplets. *Phys. Fluids* **34** (6), 063309.

JAISWAL, M., DUDHE, R. & SHARMA, P.K. 2015 Nanoemulsion: an advanced mode of drug delivery system. *3 Biotech.* **5** (2), 123–127.

JESUS, W.C., ROMA, A.M. & CENICEROS, H.D. 2018 Deformation of a sheared magnetic droplet in a viscous fluid. *Commun. Comput. Phys.* **24** (2), 332–355.

JI, Y., DAI, Y., CHEN, D., GAN, C., WANG, L. & FENG, L. 2021 Precise control of ferrofluid droplet robot in 3-D vascular model. In *2021 WRC Symposium on Advanced Robotics and Automation (WRC SARA)*, pp. 122–127. IEEE. https://ieeexplore.ieee.org/document/9612669.

JIANG, G.-S. & PENG, D. 2000 Weighted ENO schemes for Hamilton–Jacobi equations. *SIAM J. Sci. Comput.* **21** (6), 2126–2143.

JIANG, H., SHENG, Y. & NGAI, T. 2020 Pickering emulsions: versatility of colloidal particles and recent applications. *Curr. Opin. Colloid Interface Sci.* **49**, 1–15.

KENNEDY, M.R., POZRIKIDIS, C. & SKALAK, R. 1994 Motion and deformation of liquid drops, and the rheology of dilute emulsions in simple shear flow. *Comput. Fluids* **23** (2), 251–278.

KERNER, E.H. 1956 The elastic and thermo-elastic properties of composite media. *Proc. Phys. Soc.* **69** (8), 808–813.

KIM, K.-M., OH, H.M. & LEE, J.H. 2020 Controlling the emulsion stability of cosmetics through shear mixing process. *Korea-Aust. Rheol. J.* **32** (4), 243–249.

LIAO, H., LI, S., LIU, C. & TAO, G. 2020 Rheological investigation with Palierne's model on a polystyrene/nylon 6 blending melt compatibilized by a polystyrene grafted maleic anhydride. *Open J. Org. Polym. Mater.* **10** (2), 17–25.

LIU, Q., LI, H. & LAM, K.Y. 2018 Optimization of deformable magnetic-sensitive hydrogel-based targeting system in suspension fluid for site-specific drug delivery. *Mol. Pharm.* **15** (10), 4632–4642.

MAFFETTONE, P.L. & MINALE, M. 1998 Equation of change for ellipsoidal drops in viscous flow. *J. Non-Newtonian Fluid Mech.* **78** (2), 227–241.

MANDAL, S., SINHA, S., BANDOPADHYAY, A. & CHAKRABORTY, S. 2018 Drop deformation and emulsion rheology under the combined influence of uniform electric field and linear flow. *J. Fluid Mech.* **841**, 408–433.

MAPHOSA, Y. 2018 *Factors Affecting the Stability of Emulsions Stabilised by Biopolymers*. IntechOpen.

MCADAMS, A., SIFAKIS, E. & TERAN, J. 2010 A parallel multigrid poisson solver for fluids simulation on large grids. In *Eurographics/ACM SIGGRAPH symposium on Computer Animation* (ed. M. Popovic & M. Otaduy), pp. 65–73. The Eurographics Association.

MEFFORD, O.T., WOODWARD, R.C., GOFF, J.D., VADALA, T.P., ST. PIERRE, T.G., DAILEY, J.P. & RIFFLE, J.S. 2007 Field-induced motion of ferrofluids through immiscible viscous media: testbed for restorative treatment of retinal detachment. *J. Magn. Magn. Mater.* **311** (1), 347–353.

OLDROYD, J.G. & TAYLOR, G.I. 1955 The effect of interfacial stabilizing films on the elastic and viscous properties of emulsions. *Proc. R. Soc. Lond.* A **232** (1191), 567–577.

OLDROYD, J.G. & WILSON, A.H. 1950 On the formulation of rheological equations of state. *Proc. R. Soc. Lond.* A **200** (1063), 523–541.

OLDROYD, J.G. & WILSON, A.H. 1953 The elastic and viscous properties of emulsions and suspensions. *Proc. R. Soc. Lond.* A **218** (1132), 122–132.

OLIVEIRA, T.F. & CUNHA, F.R. 2015 Emulsion rheology for steady and oscillatory shear flows at moderate and high viscosity ratio. *Rheol. Acta* **54** (11), 951–971.

OSHER, S. & SETHIAN, J.A. 1988 Fronts propagating with curvature-dependent speed: algorithms based on Hamilton–Jacobi formulations. *J. Comput. Phys.* **79** (1), 12–49.

OSHER, S.J. & FEDKIW, R. 2003 *Level Set Methods and Dynamic Implicit Surfaces*. Applied Mathematical Sciences, vol. 153. Springer.

PAL, R. 2011 Rheology of simple and multiple emulsions. *Curr. Opin. Colloid Interface Sci.* **16** (1), 41–60.

PALIERNE, J.F. 1990 Linear rheology of viscoelastic emulsions with interfacial tension. *Rheol. Acta* **29** (3), 204–214.

PENG, D., MERRIMAN, B., OSHER, S., ZHAO, H. & KANG, M. 1999 A PDE-based fast local level set method. *J. Comput. Phys.* **155** (2), 410–438.

PIMENTA, P.H.N. & OLIVEIRA, T.F. 2021 Study on the rheology of a dilute emulsion of surfactant-covered droplets using the level set and closest point methods. *Phys. Fluids* **33** (10), 103306.

PODDAR, A., MANDAL, S., BANDOPADHYAY, A. & CHAKRABORTY, S. 2019 Electrorheology of a dilute emulsion of surfactant-covered drops. *J. Fluid Mech.* **881**, 524–550.

RAJA, R.V., SUBRAMANIAN, G. & KOCH, D.L. 2010 Inertial effects on the rheology of a dilute emulsion. *J. Fluid Mech.* **646**, 255–296.

RAY, A., VARMA, V.B., JAYANEEL, P.J., SUDHARSAN, N.M., WANG, Z.P. & RAMANUJAN, R.V. 2017 On demand manipulation of ferrofluid droplets by magnetic fields. *Sensors Actuators* **242**, 760–768.

ROODAN, V.A., GÓMEZ-PASTORA, J., KARAMPELAS, I.H., GONZÁLEZ-FERNÁNDEZ, C., BRINGAS, E., ORTIZ, I., CHALMERS, J.J, FURLANI, E.P. & SWIHART, M.T. 2020 Formation and manipulation of ferrofluid droplets with magnetic fields in a microdevice: a numerical parametric study. *Soft Matt.* **16** (41), 9506–9518.

ROSA, A.P. & CUNHA, F.R. 2019 The influence of dipolar particle interactions on the magnetization and the rotational viscosity of ferrofluids. *Phys. Fluids* **31** (5), 052006.

ROSA, A.P. & CUNHA, F.R. 2020 Shear rate dependence of viscosity and normal stress differences in ferrofluids. *J. Magn. Magn. Mater.* **499**, 166184.

ROSENSWEIG, R.E. 2013 *Ferrohydrodynamics*. Courier Corporation.

SEN, U., CHATTERJEE, S., SEN, S., TIWARI, M.K., MUKHOPADHYAY, A. & GANGULY, R. 2017 Dynamics of magnetic modulation of ferrofluid droplets for digital microfluidic applications. *J. Magn. Magn. Mater.* **421**, 165–176.

SHU, C.-W. & OSHER, S. 1988 Efficient implementation of essentially non-oscillatory shock-capturing schemes. *J. Comput. Phys.* **77** (2), 439–471.

SIQUEIRA, I.R., REBOUÇAS, R.B., OLIVEIRA, T.F. & CUNHA, F.R. 2017 A new mesh relaxation approach and automatic time-step control method for boundary integral simulations of a viscous drop. *Intl J. Numer. Meth. Fluids* **84** (4), 221–238.

SPATAFORA-SALAZAR, A., LOBMEYER, D., DA CUNHA, L.H.P., JOSHI, K. & BISWAL, S.L. 2021 Hierarchical assemblies of superparamagnetic colloids in time-varying magnetic fields. *Soft Matt.* **17** (5), 1120–1155. The Royal Society of Chemistry.

SUSSMAN, M. & FATEMI, E. 1999 An efficient, interface-preserving level set redistancing algorithm and its application to interfacial incompressible fluid flow. *SIAM J. Sci. Comput.* **20** (4), 1165–1191.

SUSSMAN, M., FATEMI, E., SMEREKA, P. & OSHER, S. 1998 An improved level set method for incompressible two-phase flows. *Comput. Fluids* **27** (5–6), 663–680.

TAYLOR, G.I. 1932 The viscosity of a fluid containing small drops of another fluid. *Proc. R. Soc. Lond.* A **138** (834), 41–48.

TÉMAM, R. 1969a Sur l'approximation de la solution des équations de navier-stokes par la méthode des pas fractionnaires (i). *Arch. Rat. Mech. Anal.* **32** (2), 135–153.

TÉMAM, R. 1969b Sur l'approximation de la solution des équations de navier-stokes par la méthode des pas fractionnaires (ii). *Arch. Rat. Mech. Anal.* **33** (5), 377–385.

VANANROYE, A., VAN PUYVELDE, P. & MOLDENAERS, P. 2006 Effect of confinement on droplet breakup in sheared emulsions. *Langmuir* **22** (9), 3972–3974.

VARMA, V.B., RAY, A., WANG, Z.M., WANG, Z.P. & RAMANUJAN, R.V. 2016 Droplet merging on a lab-on-a-chip platform by uniform magnetic fields. *Sci. Rep.* **6** (1), 1–12.

VLAHOVSKA, P.M. 2011 On the rheology of a dilute emulsion in a uniform electric field. *J. Fluid Mech.* **670**, 481–503.

VLAHOVSKA, P.M., BŁAWZDZIEWICZ, J. & LOEWENBERG, M. 2009 Small-deformation theory for a surfactant-covered drop in linear flows. *J. Fluid Mech.* **624**, 293–337.

VOLTAIRAS, P.A., FOTIADIS, D.I. & MASSALAS, C.V. 2001 Elastic stability of silicone ferrofluid internal tamponade (SFIT) in retinal detachment surgery. *J. Magn. Magn. Mater.* **225** (1–2), 248–255.

WANNABORWORN, S., MACKLEY, M.R. & RENARDY, Y. 2002 Experimental observation and matching numerical simulation for the deformation and breakup of immiscible drops in oscillatory shear. *J. Rheol.* **46** (5), 1279–1293.

ZHANG, J., HASSAN, M.R., RALLABANDI, B. & WANG, C. 2019 Migration of ferrofluid droplets in shear flow under a uniform magnetic field. *Soft Matt.* **15** (11), 2439–2446.